

Sensitivity of Bow-Echo Simulation to Microphysical Parameterizations

REBECCA D. ADAMS-SELIN

Department of Atmospheric Science, Colorado State University, Fort Collins, Colorado, and Atmospheric and Environmental Research, Inc., Lexington, Massachusetts

SUSAN C. VAN DEN HEEVER AND RICHARD H. JOHNSON

Department of Atmospheric Science, Colorado State University, Fort Collins, Colorado

(Manuscript received 5 October 2012, in final form 9 May 2013)

ABSTRACT

The sensitivity of a case study bow-echo simulation to eight different microphysical schemes in the Weather Research and Forecasting model was tested, with a focus on graupel parameter characteristics. The graupel parameter in one scheme was modified to have a larger mean size and faster fall speed to represent hail (“hail like”). The goal of the study was to measure the sensitivity of five parameters that are important to operational forecasters to graupel properties: timing of bowing development, system speed, wind gusts, system areal coverage, and accumulated precipitation.

The time each system initiated bowing varied by as much as 105 min. Simulations containing graupel with smaller mean size and slower fall speed (“graupel like”) bowed earlier due to increased microphysical cooling and stronger cold pools. These same systems had reduced precipitation efficiency, producing a peak storm-total accumulation of 36 mm, compared to a hail-like peak value of 237 mm, and observed a peak value of 53 mm. Faster-falling hail-like hydrometeors reached the surface with minimal melting, producing the largest accumulations. Graupel-like systems had 10-m wind gusts 73% stronger compared to hail-like systems, due to stronger low-level downdrafts. Systems with a smaller mean graupel size were 19% faster, also due to increased microphysical cooling. The size of the convective region varied by 150%, although this was partially due to scheme differences other than the graupel parameter.

The significant differences in bow-echo characteristics produced by graupel property variations in convective-resolving models emphasize careful microphysical parameterization design. These sensitivities have forecasting implications, as graupel characteristics vary depending on the ambient environment and other factors. Detailed observations of graupel properties are recommended.

1. Introduction

Increased computational power has led to the operational use of convection-resolving models. Within these models, bulk microphysical parameterization schemes are used to successfully predict hydrometeor and precipitation distributions within convective systems of multiple organizational types such as squall lines and supercells (Molthan et al. 2008; Luo et al. 2010; Hong et al. 2010). However, it has similarly been noted that simple modifications of these microphysical parameterizations can cause large differences in the resultant

convective simulation (Nicholls 1987; Tao and Simpson 1989; Fovell and Ogura 1988; Szeto and Cho 1994; Yang and Houze 1995; Gilmore et al. 2004b; van den Heever and Cotton 2004; Cohen and McCaul 2006; Luo et al. 2010). Aspects of convection important to forecasting, such as the organization, intensity, and areal coverage of the convection, as well as the system speed, are particularly sensitive to such modifications.

For example, the inclusion of ice as a microphysics class produced a more realistic stratiform precipitation region in both size and intensity in multiple squall-line simulations (Nicholls 1987; Tao and Simpson 1989; Fovell and Ogura 1988; Szeto and Cho 1994). The squall-line cold pool was much stronger due to additional cooling by melting, thereby producing more intense convection and a faster system (Fovell and Ogura 1988; Szeto and Cho 1994). Replacing the graupel class with a hail class in

Corresponding author address: Rebecca D. Adams-Selin, HQ Air Force Weather Agency, 16th Weather Squadron, 101 Nelson Dr., Offutt AFB, NE 68113.
E-mail: rebecca.selin.ctr@offutt.af.mil

other squall-line simulations resulted in a much smaller stratiform region due to faster particle fall speeds (Yang and Houze 1995; Luo et al. 2010; Morrison and Milbrandt 2011; Bryan and Morrison 2012). The faster fall speeds also meant less time for melting and evaporation, and thus reduced cooling rates and a weaker cold pool, and correspondingly slower system (Szeto et al. 1988; Szeto and Cho 1994; Adams-Selin et al. 2013).

Supercell simulations have been similarly affected. Use of graupel instead of hail in idealized supercell simulations resulted in stronger updrafts due to more latent heat release from increased deposition and accretion rates of the smaller, more numerous graupel particles (Gilmore et al. 2004b); the stronger updrafts resulted in more intense convection. Increasing the mean size of the hail class resulted in less collection and less evaporation and hence warmer cold pools (van den Heever and Cotton 2004; Cohen and McCaul 2006). These systems had a slower propagation speed.

Total accumulated precipitation is also strongly affected by the characteristics of the microphysics scheme utilized. Johnson et al. (2011) found that for short-term forecasts (less than 12 h) changes in the microphysical parameterization scheme affected the simulated hourly accumulated precipitation more than either the boundary layer parameterization or model dynamic core. Precipitation seems particularly sensitive to changes to the graupel (or hail, depending on the scheme) class characteristics; changes to this parameter produced the largest resultant variations in total precipitation in previous studies (Gilmore et al. 2004b; van Weverberg et al. 2011a). Fovell and Ogura (1988) noted that at least in 2D simulations, melting graupel/hail was the largest source of rainwater.

When microphysics schemes with graupel only were used in squall-line simulations, a significant decrease in precipitation efficiency and accumulation resulted in comparison to simulations with only hail (McCumber et al. 1991; Luo et al. 2010; Morrison and Milbrandt 2011; Bryan and Morrison 2012). The total precipitation coverage, however, increased in area, in both squall-line and supercell simulations (van den Heever and Cotton 2004; Gilmore et al. 2004b; van Weverberg et al. 2011b). This result was highlighted even more with microphysics schemes that do not have graupel as a frozen precipitation class; slow snowflake terminal velocities resulted in very widespread, light rainfall (Liu and Moncrieff 2007). Use of a microphysics scheme that explicitly predicted dual moments of the graupel size distribution (e.g., mixing ratio and total number concentration) allowed the scheme to reduce the concentration of small hydrometeors during the simulation, thereby essentially increasing their mean size (van Weverberg et al. 2012;

Bryan and Morrison 2012). Similarly to the processes discussed previously, this resulted in less evaporation, higher precipitation efficiency, and increased precipitation accumulation.

Finally, microphysics scheme changes also affect the convective organization, particularly the transition of a linear system to a bow echo. The effect of changes in the mean graupel hydrometeor size in idealized bow-echo simulations was examined by Adams-Selin et al. (2013). As in earlier studies, a decrease in the mean graupel size led to increased evaporation and melting rates. This subsequently increased the strength and depth of the cold pool, and strengthened the midlevel pressure gradient and rear-to-front system flow. Due to the increased mobility of the smaller graupel hydrometeors, peak cooling rates also shifted rearward within the system. These effects combined to aid the descent of the rear-to-front flow to the surface farther behind the convective line, further tilting the convective updraft rearward and allowing bowing to promptly develop.

Thus, it is known that changes in the frozen hydrometeor characteristics of the microphysics scheme will affect the timing of new bowing development within idealized simulation, and, therefore, probably affect typical accompanying features such as surface wind gusts as well. Naturally, other features of the system, such as accumulated precipitation, stratiform/convective area coverage, and system speed will also be affected by these same changes, as was observed in squall lines and supercells in the studies discussed above.

Many of these previous studies were idealized simulations. Those that did focus on case study simulations were primarily interested in either longer-term statistical verification (Jankov et al. 2005; Liu and Moncrieff 2007; Schwartz et al. 2010) or the individual dynamics occurring within that particular case study (McCumber et al. 1991; Luo et al. 2010; van Weverberg et al. 2011a). Little research has focused on the sensitivity of operationally forecasted fields to these microphysical variations, particularly in comparison to observations.

The goal of this work is to quantify the variability of five different forecasting parameters related to new bowing development that can be expected from changes to the microphysics scheme—specifically, the graupel parameter. The five parameters are 1) timing of new bowing, 2) maximum 10-m wind gust speed, 3) system propagation speed, 4) convective and stratiform areal coverage, and 5) total accumulated precipitation. The graupel parameter was chosen because of its large effect on microphysical cooling rates, as already noted in previous studies. To achieve this goal, a variety of microphysics schemes and parameter settings within the Weather Research and Forecasting (WRF) model were used to simulate

a case study of a bow echo that occurred over Oklahoma, with comparison to observations to aid in the quantification.

Section 2 describes the experiment and model design, as well as the specific microphysical variations. A review of the case study being simulated is presented in section 3. Section 4 discusses the sensitivity of the five operational parameters to microphysical changes, and section 5 provides the conclusions.

2. Methodology

a. Model setup

The Advanced Research core of the Weather Research and Forecasting (WRF-ARW) model, version 3.2.1 (Skamarock et al. 2008), was used in this study to simulate an isolated bow echo case over Oklahoma on 13 March 2003. This model was chosen as its ability to simulate case studies of mesoscale phenomena is well known. It is widely used in operational forecasting [e.g., High Resolution Rapid Refresh model, Alexander et al. (2011); National Centers for Environmental Prediction (NCEP) Short Range Ensemble Forecast (SREF) system, Du et al. (2009)], and its design easily allows microphysics modifications. This specific case was selected as it initiated and dissipated entirely within the confines of the Oklahoma Mesonet, allowing use of that dataset to better observe the system. Additionally, Adams-Selin and Johnson (2010) analyzed in detail surface observations of this system as it initiated bowing.

The initial and lateral boundary conditions for this simulation were provided by the National Centers for Environmental Prediction (NCEP) Global Forecast System Final Analysis (GFL FNL) dataset, at $1^\circ \times 1^\circ$ horizontal and 6-h temporal resolution. The NCEP Eta Model analysis and the North American Regional Reanalysis datasets were also used, but the GFL FNL data produced results closest to the observations. The model was initialized at 1200 UTC on 12 March 2003, and run for 36 h to 0000 UTC 14 March 2003. A horizontal grid spacing of 3 km was used; the domain is shown in Fig. 1. This resolution was selected as it is typical of current operational model resolutions (Kain et al. 2008). Model differences created by changes in microphysics schemes will vary at different resolutions (Bryan and Morrison 2012); thus, to inform the forecaster of expected differences, a typical operational resolution should be used.

The 35 vertical levels were stretched, with increasing resolution in the lower levels. Parameterization schemes other than microphysics include the Mellor–Yamada–Janjić boundary layer scheme (Janjić 1994), the Noah land surface model (Ek et al. 2003), the Rapid Radiative Transfer Model longwave radiation scheme (Mlawer et al. 1997), and the Goddard shortwave radiation scheme

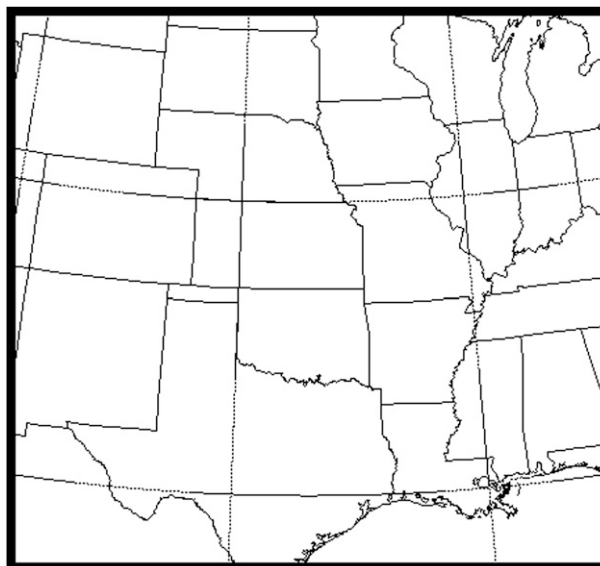


FIG. 1. WRF-ARW domain. The entire domain was run with 3-km horizontal grid spacing. Later figures will show only a subsection of the domain over eastern OK for space considerations.

(Tao et al. 2003). No convective parameterization was used, as typically grid spacing of 4 km or lower is considered convective permitting (Weisman et al. 1997). Positive-definite moisture transport was selected to avoid the positive precipitation bias associated with non-positive-definite schemes (Skamarock and Weisman 2009). This combination, in addition to the set of microphysics schemes, was chosen after considerable experimentation as it produced the most realistic convective systems when compared to observations. Additionally, this configuration is very similar to that currently used by the High Resolution Rapid Refresh (HRRR) model [Alexander et al. (2011); only difference is use of the six-layer land surface model instead of the Noah], the U.S. Air Force Weather Agency's WRF model (<http://www.meted.ucar.edu/nwp/pcu2>; only difference is the use of the Yonsei University boundary layer scheme), and the National Severe Storms Laboratory experimental high-resolution WRF (use of Dudhia shortwave radiation instead of Goddard; <http://www.nssl.noaa.gov/wrf>).

b. Microphysics and experiment design

Sensitivity tests were conducted using eight microphysics schemes available within WRF: Kessler (Kessler 1969), Ferrier (Ferrier et al. 2002), WRF single-moment five-class (WSM5; Hong et al. 2004), WRF double-moment five-class (WDM5; Lim and Hong 2010), Lin (Lin et al. 1983), WRF single-moment six-class (WSM6; Hong and Lim 2006), WRF double-moment six-class (WDM6; Lim and Hong 2010), and Morrison (Morrison et al. 2009). These specific schemes were chosen because

they include a wide range of predicted frozen hydrometeor classes and highly diverse graupel distribution characteristics, particularly in terms of the distribution intercept parameter, slope, hydrometeor density, and fall speed.

Variations in the graupel distribution intercept and slope change the mean hydrometeor size; in single-moment schemes, an increase in mixing ratio directly increases the mean size. Larger hydrometeors have a smaller surface area-to-volume ratio, which will decrease melting and evaporation rates (van den Heever and Cotton 2004; Cohen and McCaul 2006). Changes in hydrometeor density and fall speed both affect the speed at which the graupel hydrometeors leave the system. Larger, denser, and hence faster falling particles increase the downward precipitation flux (Gilmore et al. 2004b) but also allow less time for melting and evaporation. Cooling rates are correspondingly decreased as these hydrometeors fall below the melting level (van den Heever and Cotton 2004; Cohen and McCaul 2006; Adams-Selin et al. 2013). The combined effect of these two modifications (surface area-to-volume ratio and fall speed) on cooling will hereafter be referred to as the mean size effect. Removal of the graupel class or even all frozen classes altogether also significantly modifies the microphysical structure of the storm, by transferring mass into other hydrometeor classes that have different characteristics.

A full description of each of the schemes, its number of classes, and graupel intercept parameter, slope, density, and fall speed is provided in Table 1. The various graupel hydrometeor distributions and fall speeds for each scheme with a graupel class are shown in Figs. 2a and 2b, respectively. The Kessler scheme has no frozen hydrometeor classes, and is the least complex scheme used. The Morrison scheme is the most complex, and has four double-moment classes where both hydrometeor mixing ratio and total number concentration are prognostic variables. The WDM5 and WDM6 schemes include double-moment rain and cloud water distributions and cloud condensation nuclei (CCN) as a prognostic variable, allowing CCN concentration to be depleted and replenished in interaction with cloud droplets.

Within the Morrison scheme the choice can be made to switch the sixth class from graupel to hail; here, it was left as graupel. Bryan and Morrison (2012) have already examined the effect of switching this parameter in simulations of idealized squall lines. They found that simulations with a graupel class developed a wider convective line with weaker reflectivities; the hail simulation convective line was narrower with stronger reflectivities. As the Morrison graupel class is double moment, the slope and intercept of its distribution can vary, but

within two bounds (Table 1; Morrison et al. 2009). The distributions and fall speeds of the large and small bounds are both displayed in Figs. 2a and 2b.

Additional graupel sensitivity tests were conducted by varying the graupel distribution characteristics within WSM6, as in Adams-Selin et al. (2013). In that study, the graupel intercept, fall speed, and density parameters were varied to make the mean graupel hydrometeor larger, denser, faster falling, and more hail like; smaller, lighter, slower falling, and more “graupel like”; or between the two or “mid.” The parameter values used in that study were also used here and are detailed in Table 1. This study will further elucidate the effects that can be expected from these variations, specifically within operational contexts with a focus on accumulated precipitation, system areal coverage and speed, wind gusts, and timing of new bowing.

c. Convective–stratiform area determination

The simulated radar reflectivity algorithm from Stoelinga (2005) was used for reflectivity calculations. The same reflectivity algorithm was used for all simulations. The goal of this study is not to evaluate simulated radar reflectivity algorithms, but instead to compare the effects microphysics scheme modifications have on the resulting reflectivity values. Using different algorithms would allow microphysics changes to “hide” behind different reflectivity algorithms. On a more practical level, customized reflectivity algorithms were not available at the time of the study for all the microphysics schemes tested; as these are now available within WRF version 3.4.1, further future study is suggested in this regard.

Composite radar reflectivity was computed by selecting the maximum reflectivity value anywhere in the column. A threshold of 40 dBZ was selected for division of composite radar reflectivity returns into stratiform (between 15 and 40 dBZ, inclusive) or convective (greater than 40 dBZ) as in Steiner et al. (1995). [The full convective–stratiform division algorithm given in Steiner et al. (1995) was tested in this case, but the results incorrectly classified some of the stratiform region as convective, unlike the simple threshold method.] The lower threshold of 15 dBZ was selected to filter out clutter returns in the observational data. While this division is not exact, it will still allow for comparison between the observed and simulated values.

For model-simulated data, one grid point has an area of 9 km². For observed radar data, the Oklahoma City (Norman), Oklahoma (KTLX), Weather Surveillance Radar-1988 Doppler (WSR-88D) long-range composite radar reflectivity was downloaded from the National Climatic Data Center (NCDC). The National Oceanic

TABLE 1. Characteristics of the 12 unique microphysics configurations used in this study. Within the classes column, cw, ci, rw, sn, and gr represent cloud water, cloud ice, rainwater, snow, and graupel, respectively. In addition, ρ is environmental air density (kg m^{-3}), ρ_{850} is the density of the standard atmosphere at 850 hPa (kg m^{-3}), q_G is graupel mixing ratio (kg kg^{-1}), and N_G is the total concentration (m^{-3}). Mixing ratio is a prognostic value for all classes; total concentration is the second prognostic value for all double-moment classes.

Microphysics scheme	Classes	Double-moment classes	Graupel size distribution [m^{-4} ; $n_G(D_G)$]	Graupel slope (λ_G)	Graupel density (ρ_G ; kg m^{-3})	Graupel intercept (n_{0G})	Graupel fall speed (m s^{-1} ; v_G)
WSM6	cw, ci, rw, sn, gr	None	$n_{0G} \exp(-\lambda_G D_G)$	$\lambda_G = \left(\frac{\pi \rho_G t_{0G}}{\rho q_G} \right)^{1/4}$	500	4×10^6	$v_G = \frac{a_G}{6} \left(\frac{\rho_{850}}{\rho} \right)^{0.54} \frac{\Gamma(4 + b_G)}{\lambda_G^{b_G}}$ $a_G = 330, b_G = 0.8$ $a_G = 285, b_G = 0.8$ $a_G = 270, b_G = 0.8$
Hail like							
Mid							
Graupel like							
Kessler	cw, rw	None	—	—	—	—	—
Ferrier	cw, rw, sn	None	—	—	—	—	—
WSM5	cw, ci, rw, sn	None	—	—	—	—	—
WDM5	cw, ci, rw, sn	cw, rw	—	—	—	—	—
Lin	cw, ci, rw, sn, gr	None	$n_{0G} \exp(-\lambda_G D_G)$	$\lambda_G = \left(\frac{\pi \rho_G t_{0G}}{\rho q_G} \right)^{1/4}$	400	4×10^6	$v_G = \frac{a_G}{6} \left(\frac{\rho_G}{\rho} \right)^{0.5} \frac{\Gamma(4 + b_G)}{\lambda_G^{b_G}}$; $a_G = 4.67, b_G = 0.5$
WDM6	cw, ci, rw, sn, gr	cw, rw	$n_{0G} \exp(-\lambda_G D_G)$	$\lambda_G = \left(\frac{\pi \rho_G t_{0G}}{\rho q_G} \right)^{1/4}$	500	4×10^6	$v_G = \frac{a_G}{6} \left(\frac{\rho_{850}}{\rho} \right)^{0.54} \frac{\Gamma(4 + b_G)}{\lambda_G^{b_G}}$; $a_G = 330, b_G = 0.8$
Morrison	cw, ci, rw, sn, gr	rw, ci, sn, gr	$n_{0G} \exp(-\lambda_G D_G)$	$\lambda_G = \left(\frac{\pi \rho_G N_G}{\rho q_G} \right)^{1/3}$; bounds: 5×10^2 and 5×10^2	400	Variable; affected by slope bounds	$v_G = \frac{a_G}{6} \left(\frac{\rho_{850}}{\rho} \right)^{0.54} \frac{\Gamma(4 + b_G)}{\lambda_G^{b_G}}$; $a_G = 19.3, b_G = 0.37$

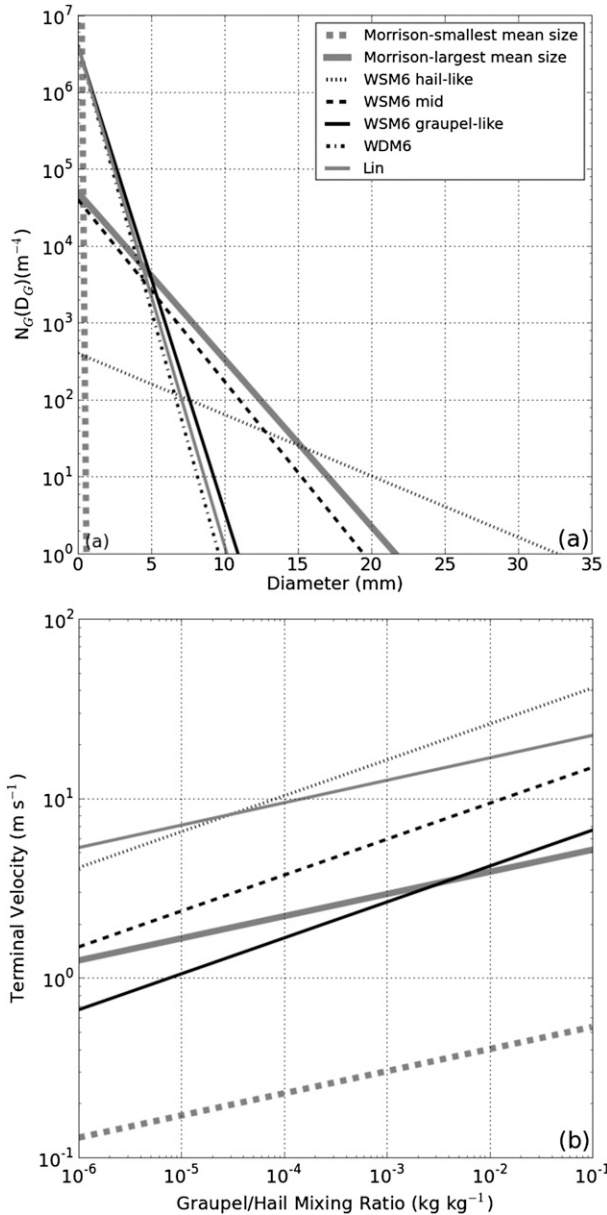


FIG. 2. (a) Graupel hydrometeor distributions for the microphysics schemes examined that have a graupel class. This assumes a graupel mixing ratio of $1 g kg^{-1}$ and air density of $1 kg m^{-3}$. Within the Morrison scheme, bounds are placed on the distribution slope; the largest and smallest values allowed are shown here. The graupel distribution in the WDM6 scheme is single moment. (b) Mass-weighted mean graupel hydrometeor terminal velocity ($m s^{-1}$) for a range of graupel mixing ratios ($kg kg^{-1}$). The WDM6 mean terminal velocity is very similar to the WSM6 graupel-like modification. The two Morrison terminal velocity functions represent the two bounds on the graupel distribution function, shown above. Temperature is fixed at 268.15 K, and pressure at 900 hPa. Calculations for graupel like, mid, and hail like are as in Adams-Selin et al. (2013).

and Atmospheric Administration (NOAA) Weather and Climate Toolkit was utilized to import the data and regrid it to approximately 100-m resolution using nearest-neighbor interpolation. Following this, nearest-neighbor interpolation was used again to reproject the data onto a grid of 3-km horizontal resolution. This method of interpretation was selected after multiple trials as it produced the gridded results closest in appearance to the observations. The number of observed and simulated convective and stratiform grid points could then be directly compared.

3. Case review

Fifteen-minute resolution WSI National Operational Weather Radar (NOWrad) mosaic base reflectivity data were obtained from the National Center for Atmospheric Research/Mesoscale and Microscale Meteorology Division’s (NCAR/MMM) archive online (<http://www.mmm.ucar.edu/imagearchive/WSI>). A description of WSI NOWrad data can be found online as well (<http://www.mmm.ucar.edu/imagearchive/WSI/docs/NOWradDescriptionWSICorp.txt>). Oklahoma Mesonet data, available every 5 min from over 110 stations across Oklahoma, were utilized to examine all other atmospheric fields.

Initiation of convection first occurred in north-central Oklahoma at 0215 UTC (not shown) within a southwest-northeast-oriented pressure trough and collocated thermal ridge (Adams-Selin and Johnson 2010). A similarly aligned convective line approximately 250 km in length formed by 0315 UTC (Fig. 3a). The system moved to the southeast at a speed of approximately $11 m s^{-1}$. A trailing stratiform precipitation region appeared at 0500 UTC (Fig. 3b), and began to develop rearward. At 0600 UTC (Fig. 3c), the center of the convective line bowed out and its speed increased to approximately $18 m s^{-1}$; stratiform precipitation filled in behind the line as it bowed. Strong 10-m wind gusts, some as high as $20 m s^{-1}$, developed at this point in association with the bowing convective line.

A secondary reflectivity maximum formed in the stratiform region at 0700 UTC, separated from the convective line by a transition zone. The bow echo continued to increase in size until 0730 UTC (Fig. 3d), at which point it started to dissipate. The cold pool and gust front associated with the decaying convective line and stratiform precipitation continued to propagate southeastward over the next 4 h. The precipitation eventually reformed into another mesoscale convective system in Louisiana.

4. Results from sensitivity tests

All of the simulations initialized a single convective cell over south-central Oklahoma, approximately 100 min

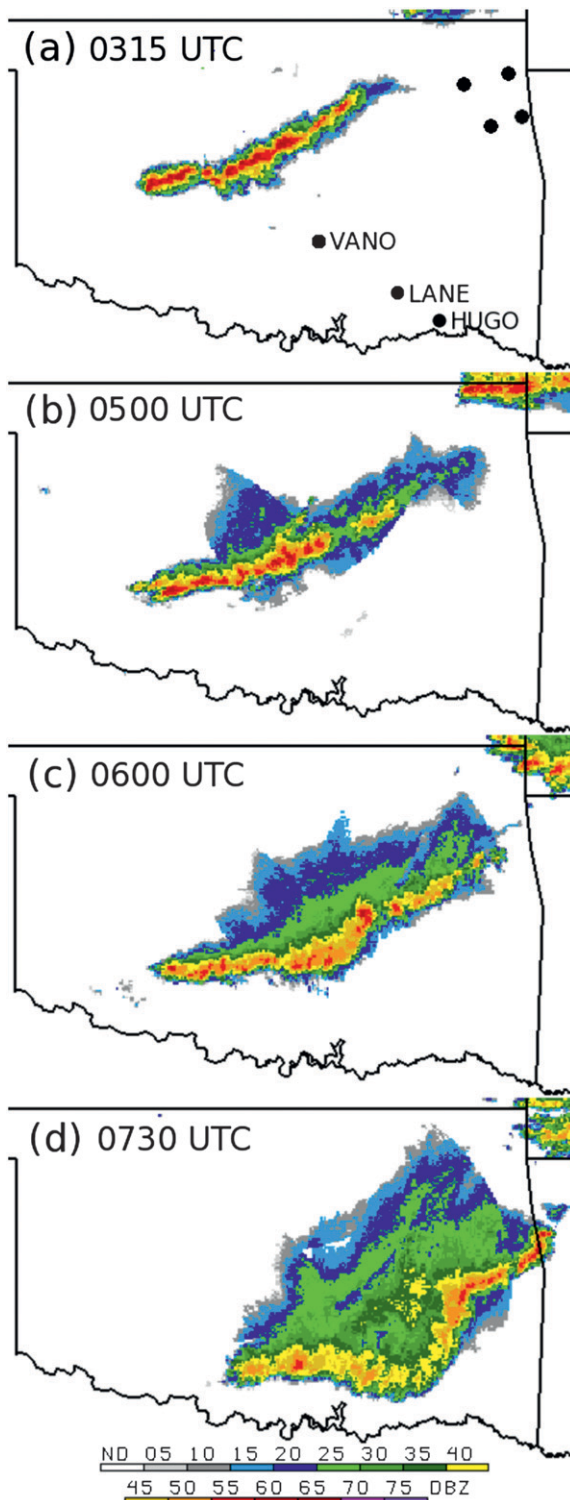


FIG. 3. WSI NOWrad composite radar reflectivity data at (a) 0315, (b) 0500, (c) 0600, and (d) 0730 UTC 13 Mar 2003. OK mesonet stations VANO, LANE, and HUGO are shown in (a); the four black dots in northeast OK are stations TAHL, WEST, PRYO, and JAYX, from which the observed environmental mean temperature was calculated.

TABLE 2. Times bowing initiated on 13 Mar 2003.

System	Time (UTC)
WSM6	
Graupel like	0545
Mid	0545
Hail like	0730
Kessler	0600
Ferrier	0615
WSM5	0620
WDM5	0615
Lin	0715
WDM6	0545
Morrison	0630
Observed	0555

later and 250 km southwest of the actual, linear, convective initiation (not shown). The location, type, and timing of the initiated convection are largely a function of the dataset used to provide the initial conditions and the planetary boundary layer parameterization and only indirectly a function of the microphysics scheme. Thus, this study will focus on the characteristics of the simulated convection after its initiation.

All simulations produced a bow echo over south-central Oklahoma somewhat faster than was observed (Table 2), making it clear that ice microphysics are not required to successfully simulate a bow echo, as was also shown in Weisman (1993). However, the simulations differ in significant details that have important forecasting implications. The convection produced in northeast Oklahoma corresponds to but is somewhat displaced from the observed convection in central Arkansas, and will not be discussed.

Five specific phenomena associated with this convective system that have an operational impact will be examined: time of bowing initiation, maximum 10-m wind gust speed, system speed, the respective areas of the convective and stratiform regions, and precipitation accumulation. Each of these will be discussed individually in the following subsections for all sensitivity test simulations.

Several microphysical parameters associated with each convective system are of importance to all five of these phenomena. Minimum surface buoyancy within the convective cold pool of the observed and simulated convection is shown later (Fig. 5) and will be discussed throughout the section. Buoyancy was calculated using

$$B = g \left[\frac{\theta - \bar{\theta}}{\bar{\theta}} + 0.61(q_v - \bar{q}_v) \right], \quad (1)$$

where g is gravitational acceleration, θ is potential temperature, q_v is water vapor mixing ratio, and the bars

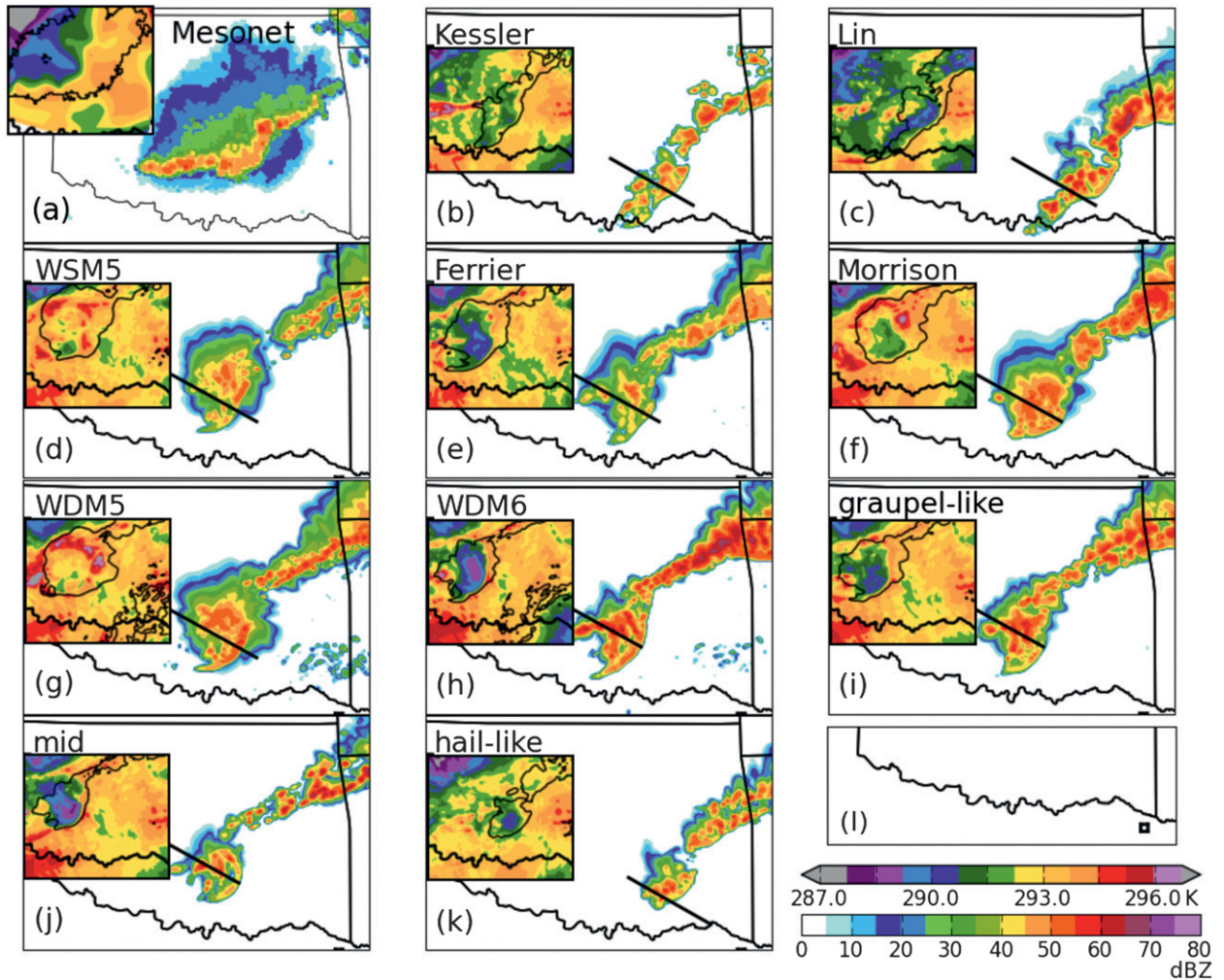


FIG. 4. Composite reflectivity, from the KTLX radar at (a) 0555 UTC and (b)–(k) model simulated at the time of maximum system updraft speed after initial bowing development. Times are given in each subfigure. Insets in each subfigure display surface potential temperature (color fill, K) at the time of bowing initiation (see Table 2 for times of bowing initiation) and the 15-dBZ simulated reflectivity contour. (l) The small black box shows the region used to calculate “environmental” conditions in the simulations.

designate environmental conditions. Values were measured at 1.5 m above ground in the Oklahoma Mesonet and 2 m in the model. Precipitation loading due to liquid and frozen hydrometeors was not included, as those measurements were not available from the Oklahoma Mesonet. Observed environmental values were an average of measurements at the Tahlequah, (TAHL), Oklahoma City West (WEST) Pryor (PRYO), and Jay (JAYX) stations in extreme eastern Oklahoma (shown as black dots in Fig. 3a). Simulated environmental conditions were mean values calculated over a 225 km² box in far north-central Texas shown in Fig. 4l; a different location was required due to the extraneous convection in northeast Oklahoma produced in each simulation.

a. Time of bowing initiation

Table 2 displays the time of bowing initiation in each simulation, and the actual time bowing developed. These times were determined subjectively by evaluating when the radius of curvature of the convective line began decreasing with time (as defined by Klimowski et al. 2004). As convection was initiated in the model 100 min later than was observed, most of the simulated systems bowed too quickly relative to the initiation. The simulated reflectivity at time of peak updraft velocity after bowing initiation in each simulation, when the bow echoes are mature, is shown in Fig. 4. The surface potential temperature field at the time of bowing is shown as an inset in each subfigure in Fig. 4, indicating the cold

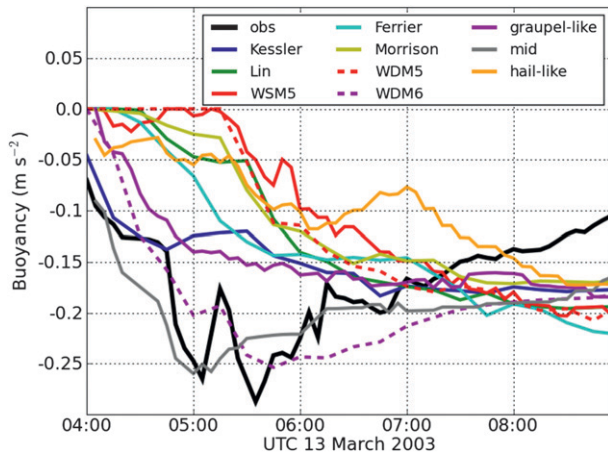


FIG. 5. Minimum surface buoyancy (m s^{-2}) of the cold pool associated with the simulated and observed (using the OK Mesonet) convective systems.

pool-driven nature of each convective system. In absolute time, the majority of the simulations initiated bowing after the observed system; this fits with the simulated convection initiating later than the actual convection.

The systems in the graupel-like and mid WSM6 configurations, and the WDM6 simulation, began bowing first at 0545 UTC. These configurations have smaller, more numerous graupel-like hydrometeors; hence, the graupel mean size effect results in increased microphysical cooling particularly early in the convective systems' lifetimes (Fig. 6a), and a deeper, more negatively buoyant cold pool (Fig. 5). Figure 6 displays the mean microphysical cooling and warming rates over the subset of the domain shown in Fig. 4 but not including the extraneous convection in northeast Oklahoma. The cold pool buoyancy can be seen in Fig. 5: the mid, graupel-like, and WDM6 cold pools all developed quickly and by 0545 UTC, the time of bowing in each case, had become quite cold. The Kessler system, whose cold pool also quickly cooled due to strong initial cooling rates (Fig. 6a), bowed comparatively early as well, about 15 min later.

The mid system reached a buoyancy minimum the earliest among all of the simulations, even faster than the WDM6 and graupel-like systems (Fig. 5). Maximum graupel size and fall speed over the domain subset are shown in Fig. 7. The faster fall speed of the mid graupel hydrometeors (Fig. 7b) allowed them to fall below the melting level first and, subsequently, melt and evaporate. While the mean cooling rates in the mid simulation were not as large as those of the graupel-like simulation (Fig. 6a), the convection and associated cooling in the mid simulation (Fig. 4j) covered less area, lowering the overall mean cooling rate. Figure 8 displays vertical

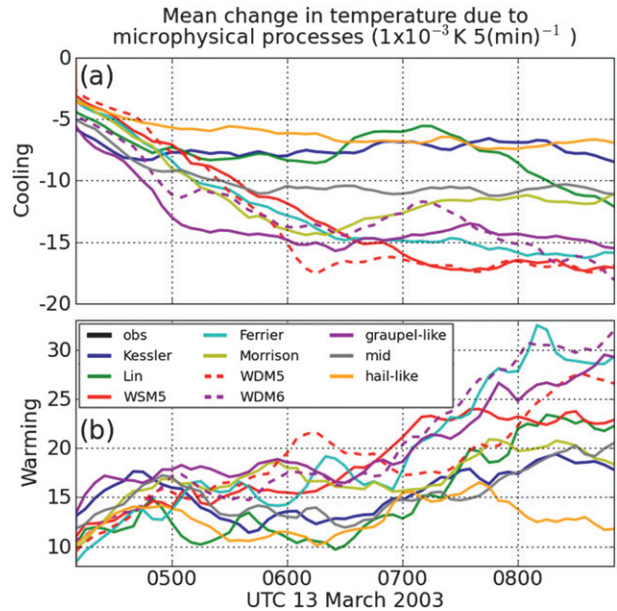


FIG. 6. Domain mean cooling (a) from evaporation, sublimation, and melting, and warming (b) from condensation, deposition, and freezing [$1 \times 10^{-3} \text{K (5 min)}^{-1}$] for all eight simulations. Line coloring is the same as in Fig. 5. “Domain” here is defined as the area of the simulation shown in Fig. 4, but without the extraneous convection in northeast OK.

cross sections of microphysical cooling rates through the newly developed bowing segment at the time of bowing initiation (Table 2). Cooling rates within the mid and graupel-like systems at the time of bowing in each were approximately equal (Figs. 8i and 8j), although the peak cooling rates in the mid system were closer to the surface.

Once the smaller graupel-like hydrometeors fell in larger numbers below the melting level later in the simulation, the mean size effect ensured large magnitudinal cooling rates (Fig. 6a) and a more negatively buoyant cold pool (Fig. 5), particularly in the WDM6 simulation. The difference in buoyancy observed between the WDM6 and graupel-like simulations will be discussed further in the next two sections. The largest magnitude cooling rates in the simulations without graupel, such as the WSM5, WDM5, and Ferrier, occur even later than those with small graupel (Fig. 6a); additional time was needed for appreciable amounts of slowly falling snow to fall below the melting level. Once this occurred, however, the mean size effect ensured large cooling rates (Fig. 6a and Figs. 8c, 8d, and 8f) and bowing development shortly thereafter (Table 2).

Figure 9 presents hydrometeor mixing ratios through vertical cross sections of the newly developed bowing segment, at the time of bowing initiation (Table 2). The increased mobility and rearward advection of the smaller graupel-like hydrometeors is evident in Figs. 9g–i,

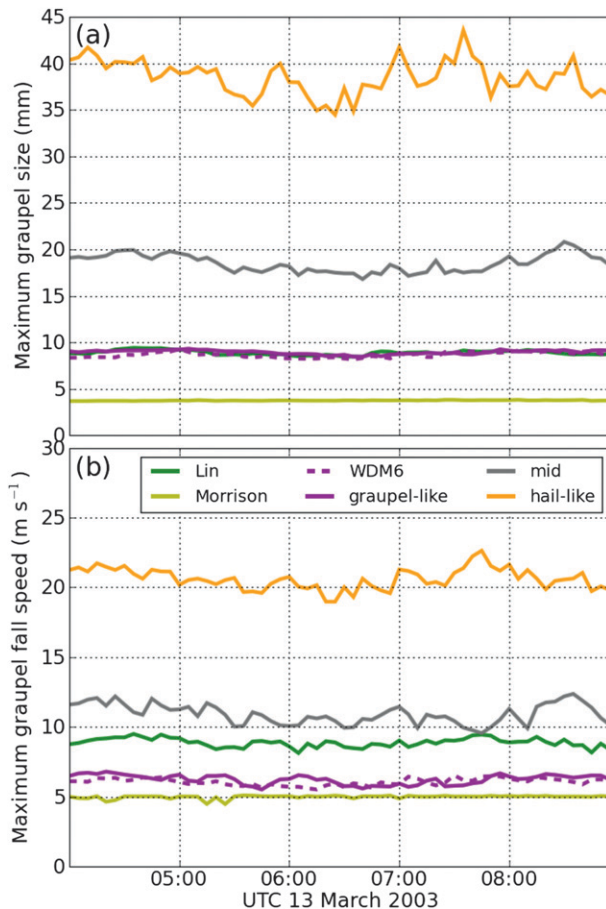


FIG. 7. (a) Maximum graupel size (mm) over the domain subset shown in Fig. 4, excluding the extraneous convection in northeast OK. (b) Maximum graupel fall speed (m s^{-1}) over the same area. Only simulations with a graupel class are shown.

compared to the smaller horizontal distribution of larger or faster-falling graupel particles in the Lin and hail-like simulations (Figs. 9b and 9j). The larger spread of graupel particles shifts the peak microphysical cooling rearward and strengthens it, shown by the stronger and wider cooling in Figs. 8g–i compared to Figs. 8b and 8j. Similar results were noted in Adams-Selin et al. (2013).

Meanwhile, the hail-like and Lin systems did not bow until over 90 min later than the graupel-like system, at 0730 and 0715 UTC, respectively. The time period between convective initiation and bowing in the observed system and these simulations was most similar, although the convective line in these simulations contained reflectivities that were approximately 10 dBZ less than observed (Figs. 4a, 4c, and 4k). The large graupel hydrometeors in these simulations resulted in reduced cooling rates through the mean size effect (Figs. 6a, 8b, and 8j) and a weaker cold pool (visible in Fig. 5). The decreased mobility and rearward advection of the larger

hail particles (Figs. 9b and 9j) ensured the peak cooling and associated downdrafts remained closer to the convective updraft. In the case of the “hail-like system,” the convection was quite weak and the bowing segment small and short lived.

The Morrison scheme system also bowed comparatively late. Because of the double-moment nature of its classes, the rain intercept parameter was allowed to decrease in the stratiform region, resulting in decreased concentrations of small raindrops compared to a single-moment scheme (Figs. 10a and 10c) and decreased evaporation rates as well (Fig. 9e; Morrison et al. 2009). The small size and slow fall speed of the graupel hydrometeors in this simulation (Fig. 7) required some time to pass before graupel fell below the melting levels in large quantities and contributed to the microphysical cooling rates. Delayed cooling, evident in Figs. 5 and 6a, resulted in later bowing development as in Adams-Selin et al. (2013).

One notable difference between this study and that of Adams-Selin et al. (2013) was in the interval between the graupel-like and hail-like simulation bowing initiation times. In that study the interval was approximately 20 min; here, the simulations differed by 105 min. The difference between minimum buoyancy values at time of bowing in the graupel-like and hail-like simulations was 0.08 m s^{-2} in this study, and 0.03 m s^{-2} in the idealized simulations of Adams-Selin et al. (2013). That study also found that the cold pool of the graupel-like system was significantly deeper. It is possible that the convective initiation method used in the idealized simulations in that study aided in simulating a much stronger hail-like system than the hail-like case study system simulated here. Thus, without a strong initiation mechanism, the role played by microphysics in affecting the timing of new bowing development was even larger.

b. 10-m wind gust speeds

It is known from van den Heever and Cotton (2004) that a decrease in the mean size of the largest frozen hydrometeor in supercell simulations results in stronger low-level downdrafts due to the increased microphysical cooling in the same location. Adams-Selin et al. (2013) found that variations in microphysical cooling can affect the descent of the rear-to-front flow within the system, as well as the timing of new bowing development. Thus, it is not unreasonable to expect surface wind gusts to vary as a result of microphysics modifications as well.

Within each simulation the maximum 10-m wind speed was calculated at every 20-s model time step and output at intervals of 5 min. Figure 11 displays this maximum wind speed from the simulations, and 10-m wind gust speed from Oklahoma Mesonet observations, at

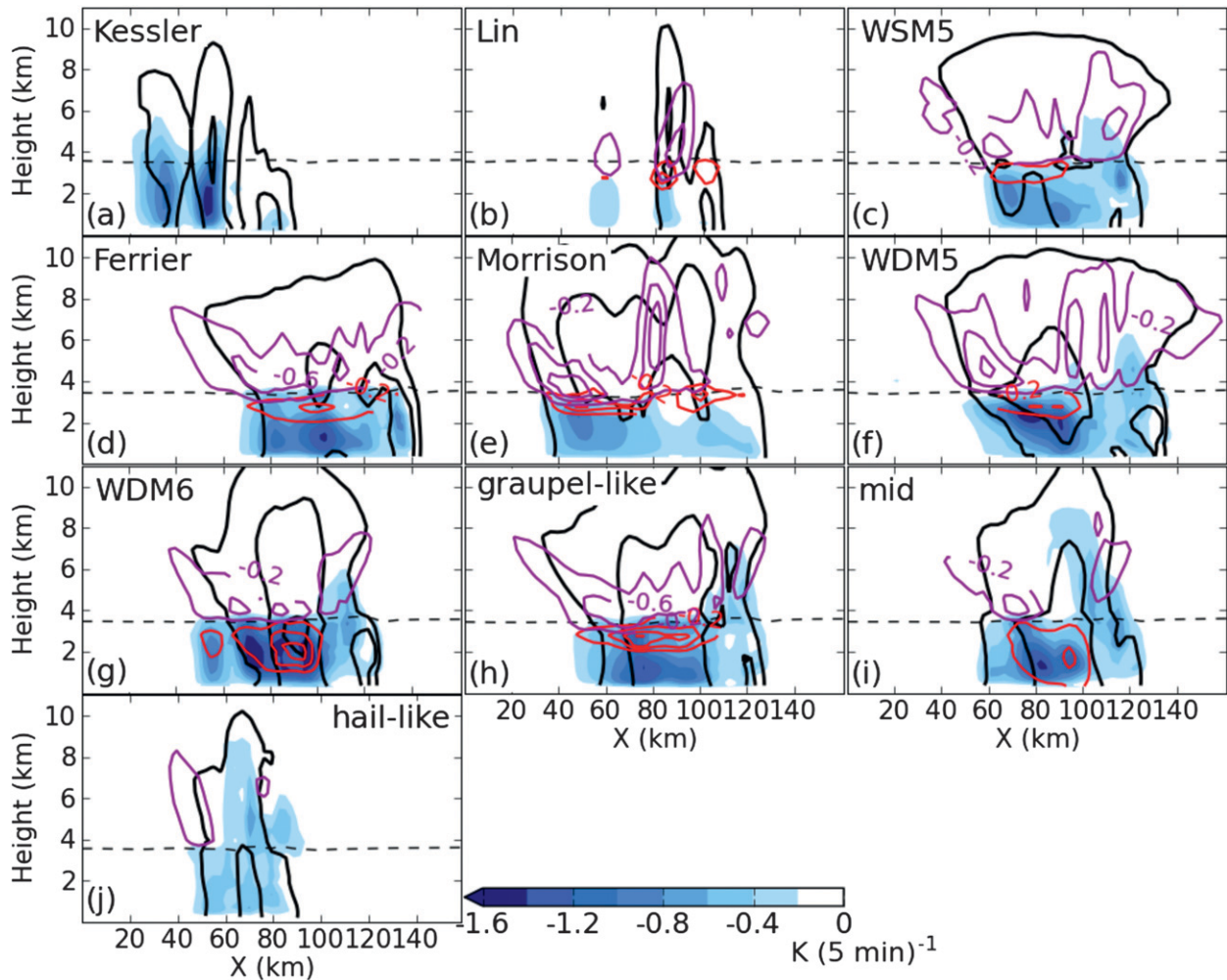


FIG. 8. Vertical cross sections of microphysical cooling due to evaporation [blue shading, K (5 min)^{-1}], melting [red, $0.4 \text{ K (5 min)}^{-1}$ starting at $0.2 \text{ K (5 min)}^{-1}$], and sublimation [purple, $0.4 \text{ K (5 min)}^{-1}$ starting at $0.2 \text{ K (5 min)}^{-1}$] at time of bowing development (times given in Table 2) for all eight simulations. The thin dashed black line is the melting level; the thick black contours are simulated reflectivity at 20, 40, and 50 dBZ. Cross sections are taken directly through the bowing segment at right angles to the convective line.

the same times as in Fig. 4. Thirty minutes after bowing was generally when wind speeds were most intense (see Table 2 for times of bowing initiation). Figure 12 displays the maximum 10-m wind speed associated with each simulated system or case observed via the mesonet. It is obvious from both of these figures that most of the simulated systems produced significantly stronger winds than were observed, particularly early in the convective lifetime. One possibility is that the observations slightly underestimated the true 10-m wind gust speed because the relatively coarse mesonet resolution (approximately 30–50 km) was unable to completely sample the highly spatially variant convective winds, compared to the higher resolution of the model (3 km). It is also possible that the model vertical resolution did not adequately resolve winds at 10 m, instead interpolating these

from a higher level. However, comparison among the simulated values is still instructive.

It is evident that the simulations with a large mean graupel size and fall speed (hail-like WSM6 configuration; Fig. 7) had weaker wind gusts (Figs. 11k and 12) than those with a smaller mean graupel size or slower fall speed (graupel like and WDM6; Figs. 11h, 11i, and 12). These smaller graupel simulations contain systems that from van den Heever and Cotton (2004) would be expected to have stronger low-level downdrafts. Increased latent cooling due to the mean size effect is evident in Figs. 8g and 8h. Increased low-level downdrafts appeared to aid in the intensification of the 10-m wind gusts associated with these simulated systems.

Early in the simulations, before bowing development, the Lin, Kessler, and mid simulations produced strong

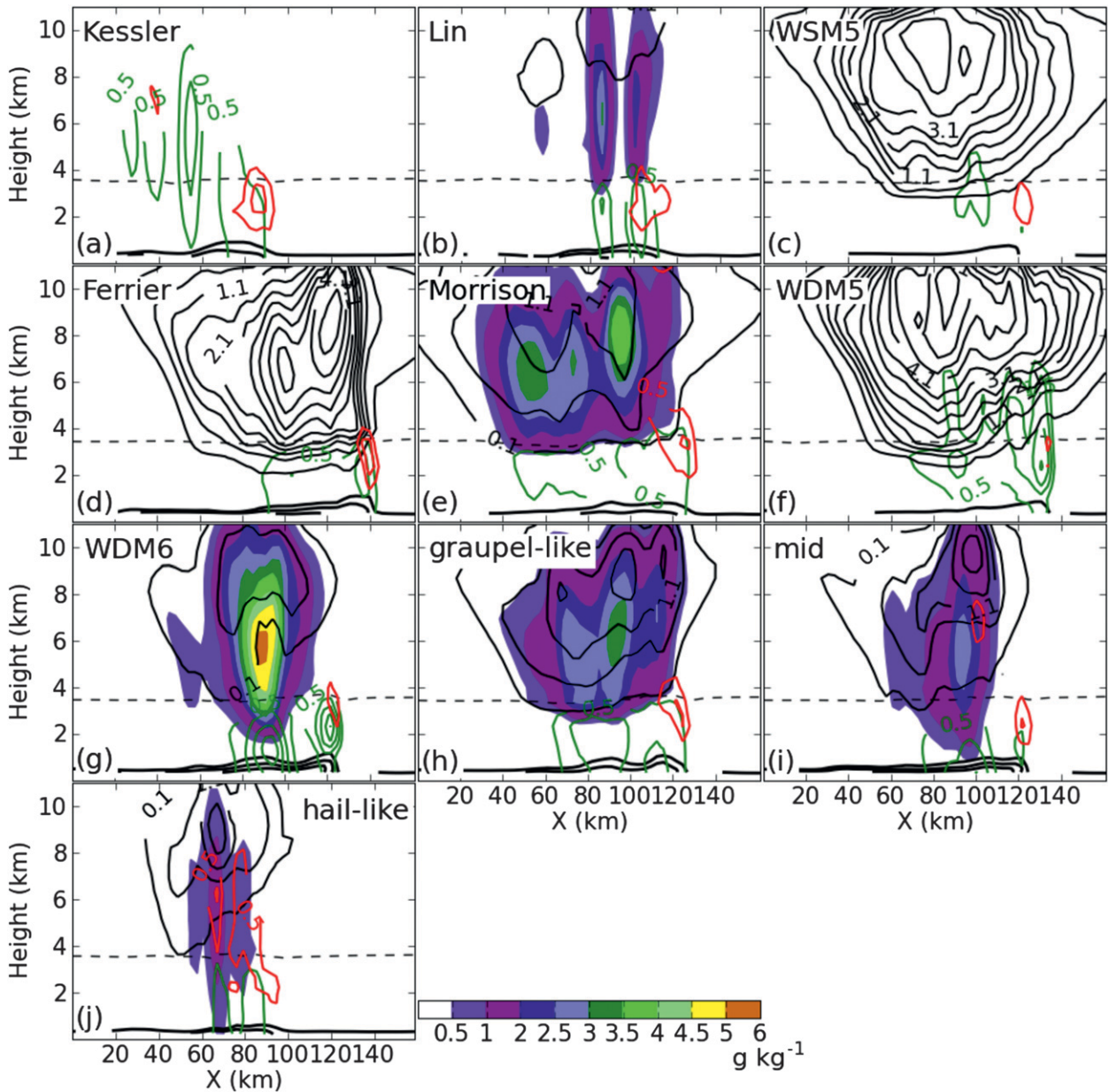


FIG. 9. Vertical cross sections of graupel (filled contours, g kg^{-1}), snow (black, 0.5 g kg^{-1} starting at 0.1 g kg^{-1}), rain (green, 0.5 g kg^{-1}), and cloud water (red, 0.5 g kg^{-1}) at time of new bowing development for all eight simulations. Thin dashed black line is the melting level; thick black lines are the potential temperature contours of the cold pool (2 K). Cross-section location as in Fig. 8.

surface winds (Fig. 12), but these had become weaker at the time of bowing and after (Figs. 11b, 11c, and 11j). The fast fall speeds of the graupel hydrometeors in these schemes (Fig. 7) and resulting increased downward precipitation flux led to strong low-level downdrafts shortly after graupel formation aloft (or, in the case of the Kessler scheme, large raindrops). The graupel (or large raindrops) fell out quickly, which is evident in the smaller mass of the hydrometeors aloft in these simulations at the times of Figs. 9a, 9b, and 9j,

resulting in reduced precipitation flux and low-level downdrafts.

Between 0600 and 0800 UTC, the time period when each system peaked in maturity as measured by updraft speed (not shown), simulations with different microphysical schemes produced peak maximum 10-m wind gust speeds varying from 16.1 m s^{-1} (hail-like simulation) to 30.5 m s^{-1} (WDM6 simulation; Fig. 12), a fluctuation of 62%. (Percentage differences were calculated by dividing the difference of the values by the mean of

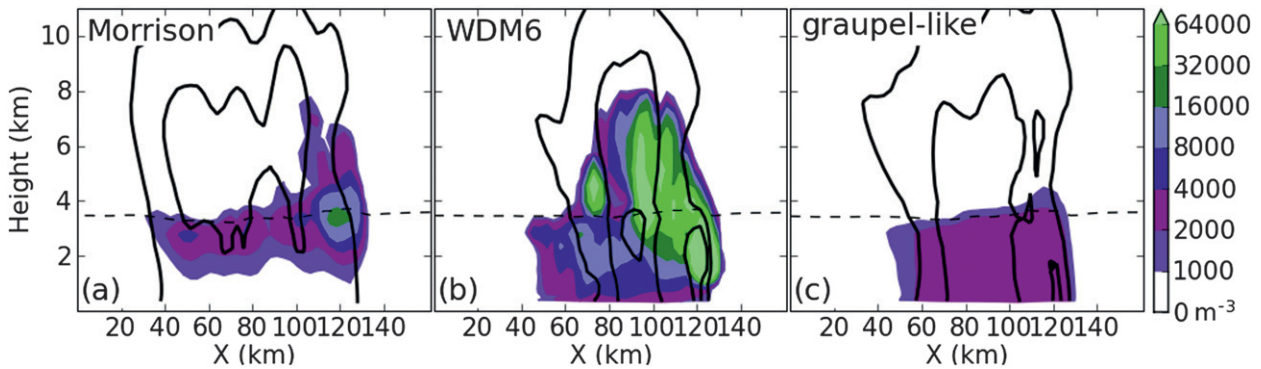


FIG. 10. Vertical cross sections of raindrop concentration (m^{-3}) at time of bowing (Table 2). (a),(b) The concentration is a prognostic variable. (c) Concentration is determined diagnostically using the drop size distribution. Thin dashed black line is the melting level; thick black lines are the 20-, 40-, and 50-dBZ simulated reflectivity contours. Cross-section location as in Fig. 8.

the values; percentage increases by dividing by the smaller value.) The variation in peak maximum wind speed due solely to graupel changes was almost as large, 53% (graupel-like peak wind speed during this time period was 27.8 m s^{-1}). As the threshold wind gust speed in National Weather Service severe thunderstorm warning criteria is approximately 26 m s^{-1} , the variation from 16.1 to 30.5 m s^{-1} has important practical forecasting implications. Thus, in addition to the already recognized model factors of initialization environment and boundary layer parameterization that significantly affect system wind gust simulation (Johnson et al. 2011), the choice of the model microphysics scheme is not insignificant.

c. System speed

System speed was determined within the simulations by evaluating the time of arrival of the convective line at Oklahoma Mesonet stations in Vanoss (VANO) and Lane (LANE) (displayed as black dots on Fig. 3a). All of the simulations produced convection that propagated in one direction, approximately a straight line between these two stations. Table 3 displays the arrival times of these simulated systems, and the calculated system speed between them. Station VANO was selected as it was approximately the point by which all the simulated systems had developed convection on its leading edge. Station LANE was selected as at that point none of the systems had yet begun to dissipate.

Based on gravity current theory, the propagation speed of a mesoscale convective system depends on the depth and strength of its cold pool (Charba 1974). The more intense the cold pool, the faster the system speed. Because all simulations in this study were initialized with the same environmental conditions, the difference in system speed can be almost entirely explained by the cold pool. Unfortunately, cold pool depth could not be

measured with the Oklahoma Mesonet data, but cold pool buoyancy was available and will be discussed below.

The slowest systems were the hail-like WSM6 configuration, Kessler, and Lin simulations (Table 3). The slow speed of the Kessler simulation was unsurprising, as without ice there was no additional cooling by melting or sublimation (Figs. 6a and 8a) to add to the strength of the cold pool, consistent with results found by Nicholls (1987) and Tao and Simpson (1989) for squall lines. While initially cooling quickly, the Kessler system slowed its cooling after 0445 UTC, resulting in a slow mean system speed (Figs. 5 and 6a). Through the mean size effect, the hail-like WSM6 system had reduced microphysical cooling (Fig. 6a), resulting in a warmer cold pool (Fig. 5) and slower system speed; fast graupel fall speeds in the Lin system produced the same result (Figs. 6a and 5).

The slower comparative speeds of the WSM5 and Ferrier simulations were at first glance unexpected. Because of the lack of a graupel class in these schemes, much larger amounts of snow were produced (Figs. 9c and 9d). The small size and slow fall speed of these hydrometeors should result in large microphysical cooling rates; this was eventually the case (Figs. 6a and 5). However, as mentioned earlier, the snow fell so slowly it took some time before significant concentrations fell below the melting level, echoing the results in Adams-Selin et al. (2013). After significant amounts of snow began melting the “no graupel” systems moved faster, but as this occurred later in the system’s life cycle, the overall system speed was still relatively slow. To evaluate this hypothesis, system speed was also calculated from LANE to the mesonet station in Hugo (HUGO, 34.03°N , 95.54°W ; southernmost black dot in Fig. 3a); the WSM5 and Ferrier systems had each increased in speed relative to the other systems (not shown).

The mid WSM6 configuration and Morrison systems were in the middle of the distribution and closest to

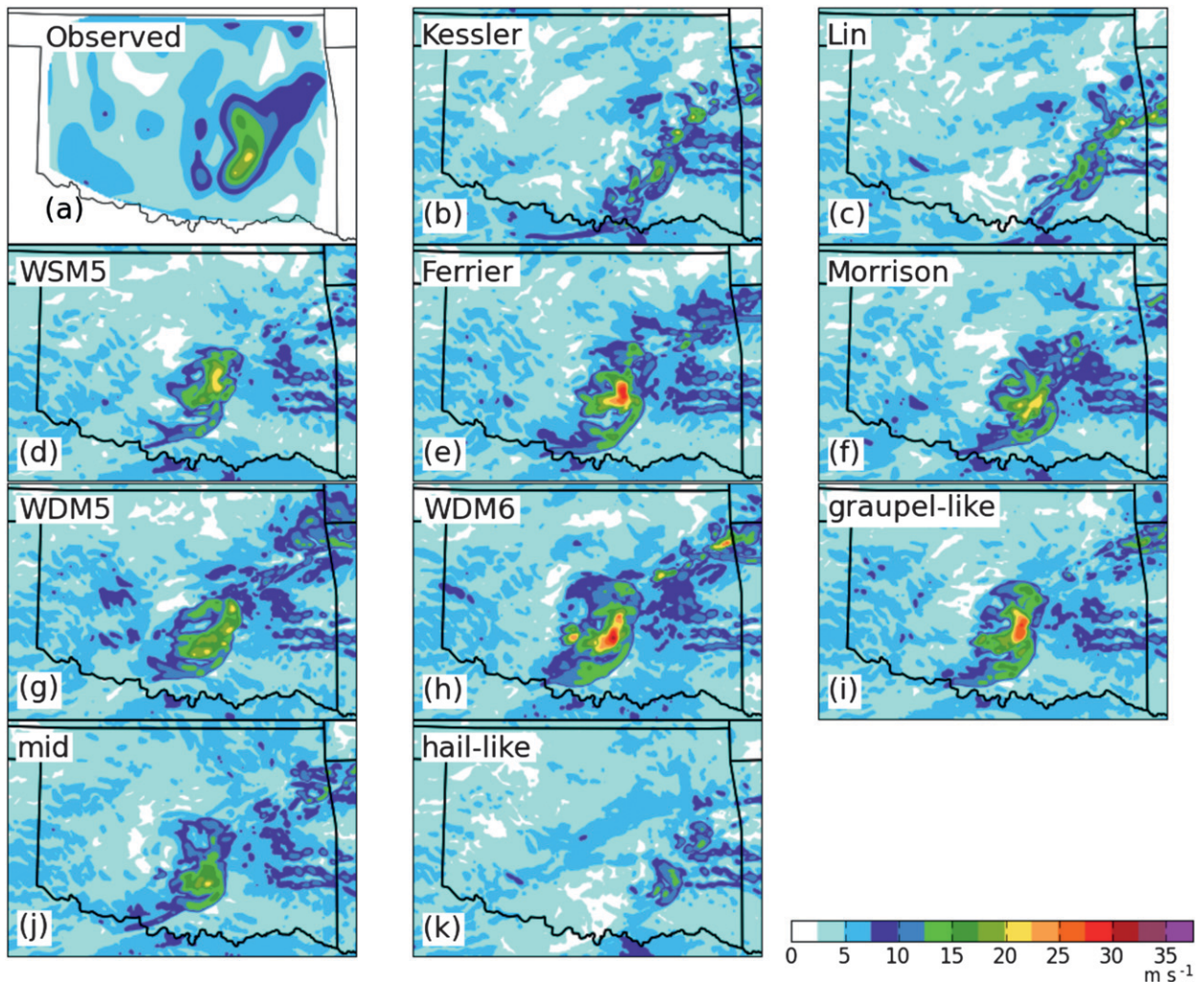


FIG. 11. The 10-m wind maximum speed (m s^{-1}), from simulations and observed from the OK Mesonet, at time given in each subfigure (same times as in Fig. 4). Observed values are peak 3-s wind speeds observed during a 5-min interval; simulated values are peak 20-s wind speeds simulated during a 5-min interval.

the observed system speed. While the cold pool associated with the mid system was very cold initially (Fig. 5), it warmed as cooling rates lessened (Fig. 6a) as more of the graupel fell out of the storm (Fig. 9i). As mentioned earlier, the graupel in the Morrison simulation was small and slow falling (Fig. 7). Thus, while large-magnitude cooling rates were eventually simulated (Fig. 8e), they were delayed (Fig. 6a), and the cold pool was relatively warmer (Fig. 5). Thus, a moderate system speed was expected and observed.

The graupel-like WSM6 configuration, WDM5, and WDM6 systems were the fastest of all the simulations. The fast speed and strong cold pool (Fig. 5) of the graupel-like configuration were expected because of the mean size effect and large cooling rates (Fig. 6a). However, the fast speeds and strong cold pools (Fig. 5) of the

two double-moment schemes (WDM5 and WDM6) systems were surprising. The double-moment nature of the rainwater distribution in WDM5 and WDM6 would typically be expected to moderate evaporation and cooling. In Morrison et al. (2009) and Bryan and Morrison (2012), the double-moment schemes used in the studies produced slower systems than the single-moment schemes. Lower concentrations of smaller rainwater hydrometeors in the stratiform region reduced evaporation and melting.

However, in studies comparing the WSM6 and WDM6 schemes, the WDM6 produced larger mass and concentrations of rain everywhere in that simulated system, not just the stratiform region (Lim and Hong 2010). Large mixing ratios (Figs. 9f and 9g) and concentrations (Fig. 10b) of rainwater were evident throughout the

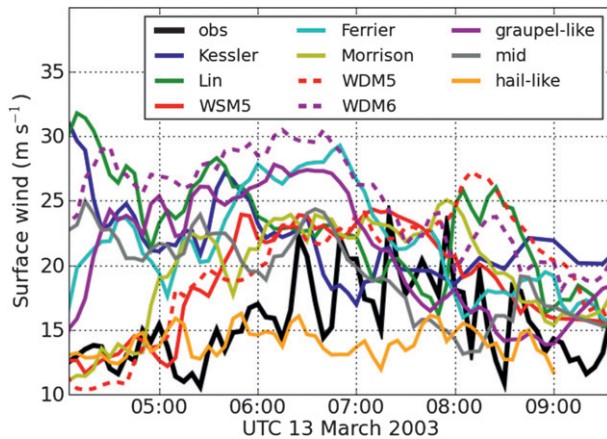


FIG. 12. Maximum 10-m wind speed within simulated or observed systems (using OK Mesonet), calculated as described in Fig. 11.

WDM5 and WDM6 systems in this study. Similar to the Lim and Hong (2010) results, enhanced snow and graupel melting processes produced the additional rainwater mass (Figs. 8f and 8g), and aided in creating a more intense cold pool (Fig. 5) and, hence, faster system speeds. Furthermore, in the double-moment schemes used in the Morrison et al. (2009) and Bryan and Morrison (2012) study, the graupel distribution was also double moment. In the WDM6 scheme, the graupel distribution is still single moment with a relatively small mean size (Fig. 7a), and thus stronger cooling occurred through the mean size effect (Fig. 6a). The WSM6 and WDM6 configurations in the 2010 Hazardous Weather Testbed Spring Experiment produced similarly intense cold pools and faster system speeds, as measured by the south- and eastward displacement of forecast precipitation compared to the observations (Clark et al. 2012).

The microphysics changes produced variations in system speed of 27%; changes in graupel characteristics within the WSM6 scheme produced an 18% variation. Furthermore, the times of arrival of the systems at the first selected station, before the systems reached maturity, deviated even more than the changes in system speed and could account for up to a 90-min difference. This would seem to indicate that the microphysics factors were also influential in the early stages of the systems' lifetimes, while still unorganized.

d. Convective–stratiform areal coverage

Figure 13 displays the observed and simulated areas of stratiform (Figs. 13a and 13b) and convective (Fig. 13c) precipitation, calculated as described in section 2c. Areal coverage from the spurious convection in northeast Oklahoma is not included in this calculation. It is obvious from Figs. 4 and 13 that all of the simulated systems

TABLE 3. Times on 13 Mar 2013 of the arrival of the simulated and observed convective line at OK Mesonet stations VANO and LANE, and system speeds between the two.

System	VANO arrival time (UTC)	LANE arrival time (UTC)	System speed
WSM6			
Graupel like	0540	0700	19.7
Mid	0545	0710	18.5
Hail like	0605	0740	16.5
Kessler	0555	0730	16.5
Ferrier	0615	0745	17.5
WSM5	0620	0750	17.5
WDM5	0620	0740	19.7
Lin	0645	0830	15.0
WDM6	0555	0715	19.7
Morrison	0620	0745	18.5
Observed	0545	0709	18.7

were both smaller (particularly in terms of stratiform coverage) and initiated later than the actual system. The smaller stratiform coverage area was partially due to the choice of the reflectivity algorithm. Use of an algorithm with a fixed snow intercept, instead of a variable one as used, increased the stratiform–convective ratio; unfortunately, it also introduced regions of spurious stratiform precipitation in southeast Oklahoma. The relations of the simulated areas to each other were relatively unchanged by the different reflectivity algorithms, however.

The smaller total stratiform and convective coverage area is partially due to the simulations initiating convection approximately an hour later than was observed, meaning the simulated convection had not had as much time to develop. In addition, the simulated systems originally initiated as an individual cell, and only later organized into the larger, linear systems seen in Fig. 4. It is also already known that the underestimation of the convective–stratiform region size ratio is a common problem when simulating convection (Luo et al. 2010). However, even noting all of these differences, it is still instructive to compare the trends of the observed and simulated precipitation areas.

The size of the stratiform region associated with each simulated system largely depends upon the size of the hydrometeors and the strength and positive buoyancy of the front-to-rear flow within the system (Fovell and Ogura 1988; Rotunno et al. 1988; Szeto and Cho 1994; Yang and Houze 1995; Luo et al. 2010). Smaller hydrometeors can be transported more easily by the system airflow, but can also be evaporated or sublimated more easily. A balance must be struck among these processes to produce a large stratiform region. Furthermore, more positively buoyant air in the stratiform region can act to create more hydrometeors, and more easily hold them aloft.

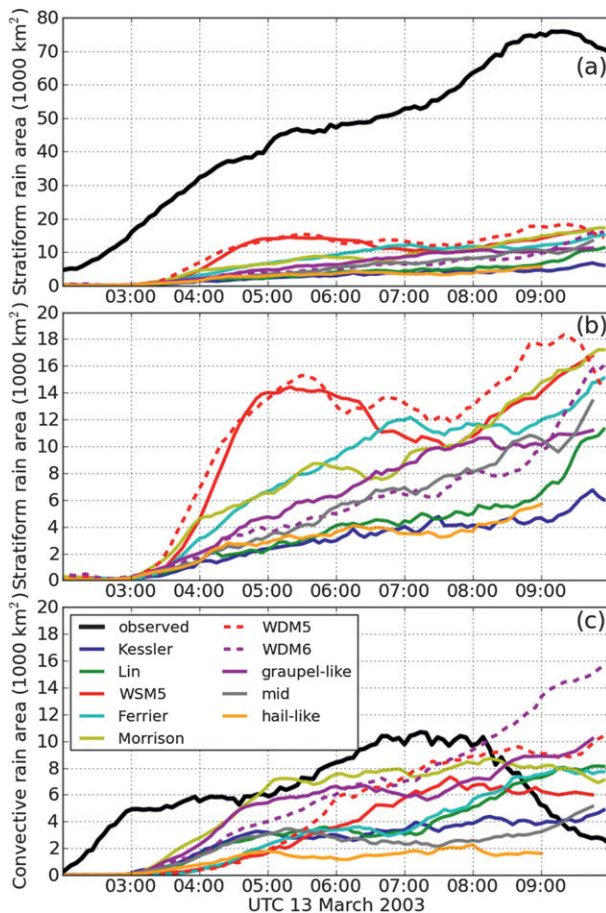


FIG. 13. Area ($\times 1000 \text{ km}^2$) of (a),(b) stratiform (zoomed in) and (c) convective precipitation, either observed (via KTLX radar) or simulated, over the course of the system's life cycle. Convective precipitation was assumed to have reflectivity values of 40 dBZ or larger; stratiform precipitation is greater than 15 dBZ but less than 40 dBZ. Additional discussion of these calculations is provided in section 2c.

Subjective comparison of the simulated bow echoes (Fig. 4) shows that the WDM5 scheme produced the largest stratiform region, although it was still smaller than the observed area. Without a graupel class, large amounts of snow were produced that were easily transported a great distance from the convective line, creating a very large stratiform shield. Additionally, both of the WDM5 and WDM6 schemes produced larger amounts of rainwater throughout the entire convective system than did any other scheme (Figs. 9f and 9g). Lim and Hong (2010) found a similar result when evaluating the effects of adding CCN as a prognostic variable, suggesting a link between prognostic CCN and the simulated system area. In the WDM5 simulation the additional freezing rainwater was added to the stratiform shield as snow (Fig. 9f), but in the WDM6 simulation this additional rainwater became graupel (Fig. 9g),

producing reflectivities of convective intensity and adding to the convective area coverage (Fig. 13c).

Four other microphysics schemes (WSM5, Ferrier, and the graupel-like and mid configurations) all produced relatively similar stratiform shield sizes, and the hail-like, Lin, and Kessler systems had the smallest stratiform regions. In the Kessler simulation, with no frozen hydrometeors, the raindrops quickly became very large and were not advected large distances from the convective line [Fig. 9a; similarly observed by Nicholls (1987), Tao and Simpson (1989), and Fovell and Ogura (1988) for squall lines]. In addition, with the lack of warming produced in association with freezing and deposition (Fig. 6b), the system updrafts and overall front-to-rear flow were not as strong (not shown), again resulting in hydrometeors not being advected as far from the convective line (similar to Szeto and Cho 1994).

The hail-like and Lin system graupel fall speeds were faster (Fig. 7b), so the hydrometeors were not advected rearward a significant distance (Figs. 9b and 9j). Evaluation of the Lin scheme by Luo et al. (2010) noted that the short graupel residence times yielded decreased condensate loading and therefore a convective updraft that peaked at higher levels aloft. The peak divergence and front-to-rear flow were therefore at higher levels as well: heights containing less ice and less buoyant air, resulting in weaker stratiform updrafts and less deposition aloft (Fig. 6b).

All of the simulations contained convective areas that were much closer to observed than the stratiform areas were, albeit lagged in time (Fig. 13c). The WDM5, WDM6, and Morrison schemes generally had the largest convective regions. For the WDM5 and WDM6 simulations, slightly smaller cloud droplet and large raindrop mixing ratios are evident in Figs. 9f and 9g; large raindrop concentrations were noted as well (Fig. 10b). Lim and Hong (2010) noted similar variations. The prognostic CCN and double-moment cloud water distributions in those schemes allowed CCN concentrations, and therefore cloud droplet concentrations, to decrease in the convective line. Increased autoconversion rates resulted, although that increase depended on the number of CCN available.

By 0900 UTC, the convective area in the WDM6 scheme in particular was $13\,293 \text{ km}^2$, approximately 4500 km^2 larger than that of the graupel-like simulation (8874 km^2). This variation was not as large as that resulting from graupel characteristics changes (a difference in 7263 km^2 between the graupel-like and hail-like simulations at 0900 UTC), but is still sizable and indicates that the effect of prognostic CCN and a double-moment cloud water class on convective area size is not insignificant. However, full consideration of CCN

and cloud water effects is beyond the scope of this study.

The Kessler system quickly developed a convective region; the simulated raindrops were not scavenged by ice crystals and grew in size rapidly (not shown). The convective region in the hail-like configuration was slowest to develop; the weak cold pool (Fig. 5) resulted in the system organizing only with difficulty. The WSM5, WDM5, and Ferrier schemes peaked in convective area later than the other graupel-inclusive schemes. The convective regions of those systems intensified and grew larger after additional cooling by melting and evaporation (Fig. 6a) was added, as the snow aloft finally fell below the melting layer in significant amounts.

The difference between peak values of stratiform region coverage in the WDM5 and the hail-like schemes, the simulations containing the largest ($18\,324\text{ km}^2$) and smallest maximum areal values ($5\,679\text{ km}^2$), respectively, was $12\,645\text{ km}^2$, or a percent difference of 105%. Given the deficiencies in simulations of stratiform regions documented in the literature (Rutledge and Houze 1987; Nicholls 1987; Szeto et al. 1988; Tao and Simpson 1989; Tao et al. 1993; Szeto and Cho 1994; Chin 1994; Gallus and Johnson 1995; Bryan and Morrison 2012), large variations in the stratiform region are unsurprising.

Peak convective region sizes differed by $13\,392\text{ km}^2$, or 150%; the peak graupel-like and hail-like convective coverage differed by $7\,920\text{ km}^2$, or 127%. Thus, it is clear that the area covered by simulated reflectivity returns is heavily dependent on the selected microphysics scheme. Microphysics scheme characteristics of variables other than graupel parameters had a larger effect here than on the other forecasting parameters: specifically, explicit prediction of cloud condensation nuclei concentration, a double-moment cloud water class, and the lack of ice as a variable. These effects are also more far reaching than just reflectivity values; cloud cover and ice or liquid water content changes also have significant radiation and surface water budget implications.

e. Accumulated precipitation

Figure 14 displays the total accumulated system precipitation of each simulation, as well as the observed values taken from the Oklahoma Mesonet and the NCEP/Environmental Modeling Center (EMC) 4-km stage IV gridded analysis. The stage IV analysis was included due to the relatively large resolution of the Oklahoma Mesonet gauge network. Every simulation produced extraneous convection over northeast Oklahoma and southeastern Arkansas, which corresponded to observed convection over central Arkansas. Table 4 provides domain-mean accumulation totals, and the percentage of the domain area with total

precipitation larger than 4 mm. Here, as in the wind gust calculations, “domain” was the domain subset shown in Fig. 4, with northeast Oklahoma excluded to remove the extraneous convection. The domain mean and area coverage of the precipitation were underforecast in all simulations, largely because the simulated systems initiated as smaller, cellular convection, as opposed to larger, linear convection.

It is obvious from Fig. 14 that 1) the choice of the microphysics scheme configuration had an enormous effect on the resulting accumulated precipitation and 2) many of the simulations significantly overforecast peak precipitation totals, although they underestimated the areal coverage. Regarding the overforecasting of peak totals, this was very likely due to the relatively large, yet currently used operationally, horizontal resolution of 3 km. Bryan and Morrison (2012) noted that as horizontal resolution decreases, more turbulence is explicitly resolved. Additionally, a larger number of smaller clouds is produced as opposed to a few large clouds, increasing the total cloud surface area. Both of these processes act to increase cloud water evaporation rates, and decrease precipitation efficiency accordingly. Thus, the schemes that produced lower precipitation totals should not necessarily be considered as having done a “better” job; if simulation resolution was decreased, those schemes could begin underpredicting.

Accumulated precipitation point maxima in each simulation vary from 36 mm in the WSM5 simulation to 237 mm in the hail-like simulation (Fig. 14), compared to the observed maximum accumulation of 53 mm. This is a 558% increase from a simulation without graupel to a simulation with hail-like graupel at current operational model resolutions. Mean precipitation over the domain subset (Table 4) ranged from 1.32 (WDM5) to 4.80 (hail like) mm, a 264% increase. Areal coverage of accumulations greater than 4 mm varied from approximately $39\,900\text{ km}^2$ (or 12% of the domain subset, WDM5) to $54\,100\text{ km}^2$ (or 17% of the domain subset, graupel like), a variation of 30%. This has serious implications for warm-season quantitative precipitation forecasting (QPF), and suggests that forecasters should be aware of which microphysics scheme with its associated biases is being used to generate a precipitation forecast.

Microphysics configurations containing large, fast-falling, more hail-like graupel hydrometeors, such as the mid and hail-like configurations, produced the largest peak and domain mean precipitation accumulations due to the mean size effect (Table 4; Figs. 14j and 14k). The fast fall speeds of the Lin scheme (Fig. 7b) also resulted in larger accumulated precipitation amounts (Fig. 14c). The areal coverage of this precipitation was smaller in these three schemes (Table 4), however, due

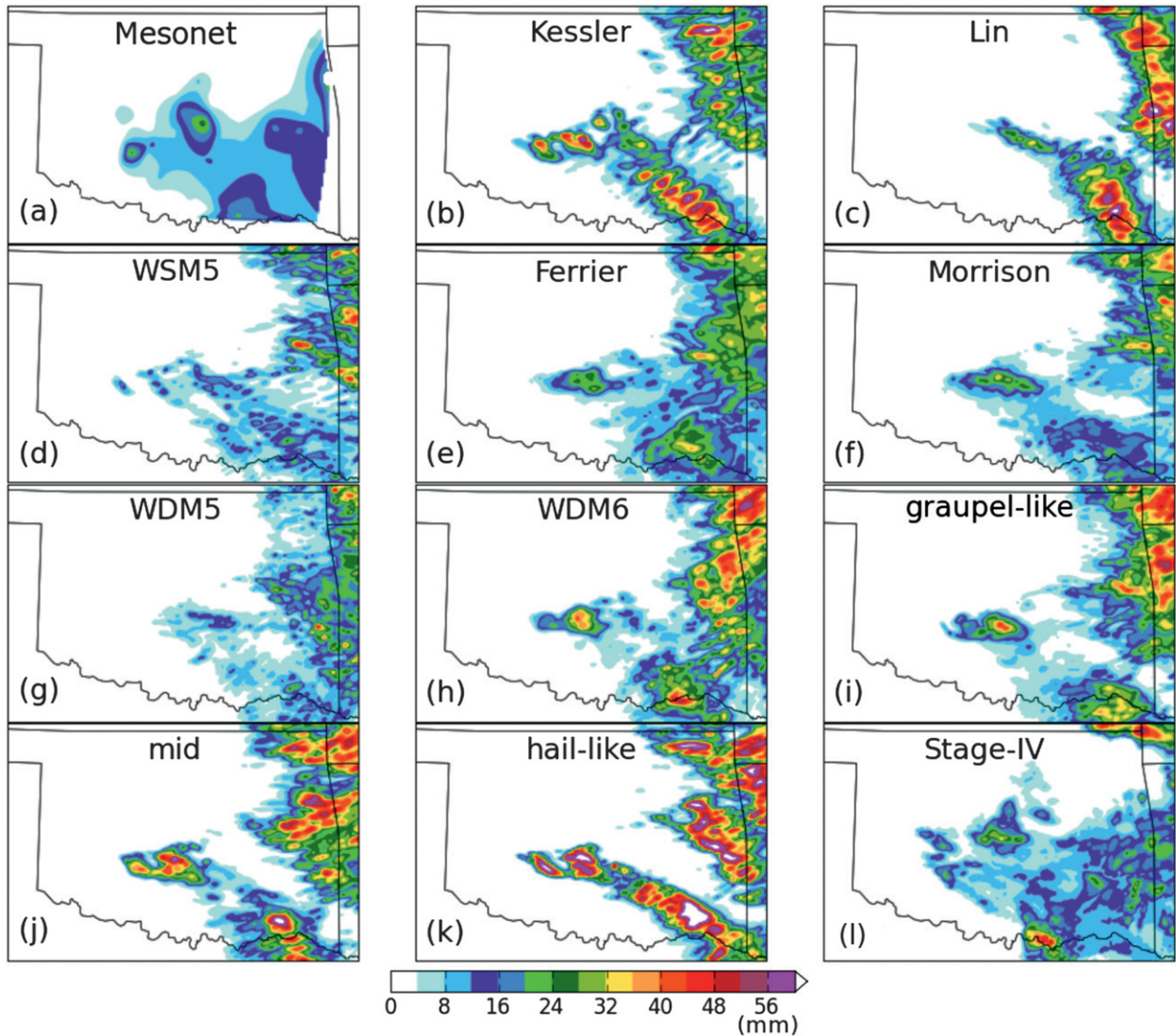


FIG. 14. Total system accumulated precipitation (mm) for (b)–(k) each simulated system, and observations from (a) the OK Mesonet and (l) NCEP stage IV gridded analysis.

to the faster graupel fall speeds (Fig. 7b). These simple changes in the graupel hydrometeor intercept parameter and fall speed alone accounted for almost all of the variation in accumulated precipitation. For example, the double-moment nature of the WDM5 and WDM6 rain distributions appeared to have little effect, in both peak and mean precipitation totals (Table 4). The larger amount of rainwater produced in these simulations (Figs. 9f and 9g) was balanced by increased evaporation (Figs. 8f and 8g) due to small mean graupel sizes (Fig. 7a) and increased raindrop concentrations (Fig. 10b).

The double-moment Morrison scheme (Fig. 14f) also did not produce more accumulated precipitation than the single-moment configurations. In Morrison et al. (2009), van Weverberg et al. (2012), and Bryan and Morrison

(2012), the double-moment Morrison scheme simulation did produce more precipitation than the simulation with a modified single-moment Morrison scheme. In those studies, the double-moment simulation allowed the concentrations of small rain hydrometeors to decrease in the stratiform region, yielding less evaporation and more precipitation. In this study, the smaller graupel size and slower fall speed in the Morrison scheme (Fig. 7) allowed more time for melting and evaporation (Fig. 8e), counteracting the decreased evaporation rates due to smaller concentrations of small raindrops (Fig. 10a). Thus, the Morrison and single-moment schemes ended up producing approximately equivalent amounts of accumulated precipitation. The advection of the slower-falling graupel hydrometeors

TABLE 4. Domain-mean accumulated precipitation (mm) and percentage of domain area with storm total precipitation of 4 mm. "Domain" is defined as area shown in Fig. 4, with the extraneous convection in northeast OK omitted. Observed values are calculated using the 4-km resolution stage IV precipitation data.

System	Domain mean	Area with accumulations > 4 mm (%)
Graupel like	2.33	16.8
Mid	2.51	15.0
Hail like	4.80	12.9
Kessler	2.33	14.4
Ferrier	2.33	16.6
WSM5	1.50	15.2
WDM5	1.32	12.4
Lin	2.78	15.3
WDM6	2.25	14.4
Morrison	1.93	16.7
Observed	3.82	30.6

did allow the system to produce a large precipitation area (Table 4).

The large values of accumulated precipitation produced by the Kessler scheme agree with the study by Gilmore et al. (2004a). In that study, the increased Kessler rainfall totals were a result of the faster raindrop production rate by cloud droplet accretion and auto-conversion. These increased raindrop production rates are a unique feature of the Kessler scheme. In the Gilmore et al. (2004a) study a comparison simulation was run using the Lin scheme with only liquid; that simulation produced approximately 40% less precipitation than the simulation using the Lin scheme that included ice. Thus, removal of ice alone would not act to increase precipitation.

In summary, the size of the graupel hydrometeors played the largest role in modifying precipitation totals in these sensitivity tests, more so than the single- or double-moment nature of the graupel or rain classes. Peak precipitation totals differed by a factor of almost 150% due to these variations; domain-mean totals by 114%.

5. Conclusions

The 13 March 2003 bow echo mesoscale convective system over Oklahoma was simulated using the Advanced Research Weather Research and Forecasting model (WRF-ARW v3.2.1). Eight different microphysics schemes were utilized to examine and quantify the differences produced by these variations within the case study simulations, specifically regarding the graupel hydrometeor class (or lack thereof). The Kessler, Ferrier, WRF single-moment five-class, WRF double-moment five-class, Lin, WRF double-moment six-class, and Morrison

schemes were used unaltered from the standard WRF settings. Three different configurations of the WRF single-moment six-class scheme were employed, modifying the graupel hydrometeor distribution intercept and density to make the hydrometeor class more graupel like or hail like.

Five operational forecasting parameters were selected to examine the resultant effects of changes to the graupel parameter on a bow echo simulation: time of initiation of bowing, 10-m wind gust speed, system speed, convective and stratiform area coverage, and total accumulated precipitation. Significant variations were observed in all of these parameters depending on the microphysical parameterization used. The schemes with smaller, more numerous, and slower-falling graupel hydrometeors produced much larger microphysical cooling rates, due to the increased surface area-to-volume ratio of the hydrometeors, and the increased time allowed for sublimation, melting, and evaporation from the slower fall speeds.

The time of bowing initiation was strongly affected. The largest impact was from the graupel-hail modifications: the graupel-like system bowed 105 min earlier than the hail-like system. As noted in Adams-Selin et al. (2013), the increased cooling associated with the graupel-like graupel hydrometeor resulted in faster development of bowing. In general, systems with smaller, lighter graupel hydrometeors also had stronger 10-m wind gusts (73% stronger), due to the increased low-level downdrafts from higher microphysical cooling rates. Peak wind gusts ranged from 16.1 to 30.5 m s⁻¹; this interval includes the National Weather Service severe thunderstorm wind gust criterion of 26 m s⁻¹. The increased cooling rates also resulted in faster system speeds (a difference of 27%).

Systems with heavier, less numerous, and faster-falling graupel (or hail like) hydrometeors had a much higher precipitation efficiency, producing peak accumulated precipitation values over 6 times larger than those in systems simulated using schemes with smaller, slower-falling, more graupel-like hydrometeors. Accumulated precipitation was by far the parameter most sensitive to graupel variations examined in this study. Changing the graupel parameter to be more graupel like or hail like had a larger effect than even switching between single- and double-moment rain or graupel distributions, or removing graupel altogether. This is particularly important when considering that the graupel intercept and fall speed parameters in current microphysics schemes are selected largely arbitrarily due to the lack of observed data and suggests that a field program or other detailed observations of these parameters is warranted.

The total size of the convective and stratiform regions also varied significantly in relation to changes in the microphysics scheme. The difference between the largest and smallest peak simulated stratiform region areas was 105%; between convective areas, it was 150%. However, the change in convective areas was also partially due to the inclusion of cloud condensation nuclei as a prognostic variable and double-moment rain and cloud water classes. Among the modified WSM6 configurations designed to test graupel sensitivity specifically, peak stratiform (convective) region sizes varied by 65% (127%).

Thus, it is clear that simple modifications to how graupel is represented within a microphysics scheme used to simulate a case study can have substantial effects on the resulting convective system. This has serious implications for operational forecasting and suggests that forecasters should be aware of which microphysical parameterization—and its associated biases—is being used to produce the model forecast being evaluated. Multiphysics ensembles should also be constructed in a way that incorporates complementary biases. For example, the WDM6 scheme has a graupel parameter with a generally small mean size and therefore strong cold pools. If that scheme is included in an ensemble, a microphysics scheme with a double-moment graupel distribution that allows for a large mean graupel size should also be included, for balance.

This work focused on effects of variations in the graupel hydrometeor class. However, it is obvious that there are multiple other factors within these microphysics schemes that affect operational parameters. Differences caused by changes in the raindrop distribution and concentration, through both single- and double-moment schemes and the introduction of prognostic cloud condensation nuclei, should be more fully examined. This is particularly needed within the ongoing work to couple microphysics schemes with the WRF chemistry model (WRF/Chem; Ward and Cotton 2011). Quantified variations and comparison to observations of many of the recent idealized hail–graupel comparison studies (Morrison and Milbrandt 2011; van Weverberg et al. 2012) would also be useful, especially the modifications of the graupel class from single to double moment, in light of the strong sensitivity to graupel changes the forecasting parameters had in this study. Finally, this case study was of a unique convective mode: other case study comparisons of different convective modes or nonconvective precipitation would also be instructive.

Acknowledgments. This research was supported by National Science Foundation Grants ATM-0500061 and AGS-0966758, and conducted under the Cooperative

Research Data Agreement between the Air Force Weather Agency and Atmospheric Environmental Research, Inc. Susan van den Heever is supported by the NSF under Grant ATM-0820557. Oklahoma Mesonet data were provided through the courtesy of the Oklahoma Mesonet, a cooperative venture between Oklahoma State University and the University of Oklahoma, and supported by the taxpayers of Oklahoma. NCEP/EMC 4-km stage IV were data provided by NCAR/EOL under sponsorship of the National Science Foundation. The WSI NOWrad data were provided by the Mesoscale and Microscale Meteorology Division of the University Corporation for Atmospheric Research (UCAR) through David Ahijevych. Computing resources were provided by the Navy Department of Defense (DoD) Supercomputing Resource Center (Navy DSRC) and the Army Research Laboratory Department of Defense Supercomputing Resource Center (ARL DSRC), which are sponsored by the DoD High Performance Computing Modernization Program. The authors thank Morris Weisman, George Bryan, and Kevin Manning of NCAR, as well as Russ Schumacher and Steven Rutledge of Colorado State University, for discussions regarding this work and assistance in using the WRF model. The comments of two anonymous reviews contributed greatly.

REFERENCES

- Adams-Selin, R. D., and R. H. Johnson, 2010: Mesoscale surface pressure and temperature features associated with bow echoes. *Mon. Wea. Rev.*, **138**, 212–227.
- , S. C. van den Heever, and R. H. Johnson, 2013: Impact of graupel parameterization schemes on idealized bow echo simulations. *Mon. Wea. Rev.*, **141**, 1241–1262.
- Alexander, C. R., S. S. Weygandt, S. G. Benjamin, T. G. Smirnova, J. M. Brown, P. Hofmann, and E. P. James, 2011: The High Resolution Rapid Refresh (HRRR): Recent and future enhancements, time-lagged ensemble, and 2010 forecast evaluation activities. Preprints, *20th Conf. on Numerical Weather Prediction*, Seattle, WA, Amer. Meteor. Soc., 12B.2. [Available online at <https://ams.confex.com/ams/91Annual/webprogram/Paper183065.html>.]
- Bryan, G. H., and H. Morrison, 2012: Sensitivity of a simulated squall line to horizontal resolution and parameterization of microphysics. *Mon. Wea. Rev.*, **140**, 202–225.
- Charba, J., 1974: Application of gravity current model to analysis of squall-line gust front. *Mon. Wea. Rev.*, **102**, 140–156.
- Chin, H. N. S., 1994: The impact of the ice phase and radiation of a midlatitude squall line system. *J. Atmos. Sci.*, **51**, 3320–3343.
- Clark, A. J., and Coauthors, 2012: An overview of the 2010 Hazardous Weather Testbed Experimental Forecast Program Spring Experiment. *Bull. Amer. Meteor. Soc.*, **93**, 55–74.
- Cohen, C., and E. W. McCaul Jr., 2006: The sensitivity of simulated convective storms to variations in prescribed single-moment microphysics parameters that describe particle distributions, sizes, and numbers. *Mon. Wea. Rev.*, **134**, 2547–2565.
- Du, J., G. Dimego, Z. Toth, D. Jovic, B. Zhou, J. Zhu, J. Wang, and H. Juang, 2009: Recent upgrade of NCEP Short-Range

- Ensemble Forecast (SREF) system. Preprints, *23rd Conf. on Weather Analysis and Forecasting/19th Conf. on Numerical Weather Prediction*, Omaha, NE, Amer. Meteor. Soc., 4A.4. [Available online at <https://ams.confex.com/ams/pdfpapers/153264.pdf>.]
- Ek, M. B., K. E. Mitchell, Y. Lin, E. Rogers, P. Grunmann, V. Koren, G. Gayno, and J. D. Tarpley, 2003: Implementation of Noah land surface model advances in the National Centers of Environmental Prediction operational mesoscale Eta model. *J. Geophys. Res.*, **108**, 8851, doi:10.1029/2002JD003296.
- Ferrier, B. S., Y. Jin, Y. Lin, T. Black, E. Rogers, and G. DiMego, 2002: Implementation of a new grid-scale cloud and precipitation scheme in the NCEP Eta Model. Preprints, *19th Conf. on Weather Analysis and Forecasting/15th Conf. on Numerical Weather Prediction*, San Antonio, TX, Amer. Meteor. Soc., 10.1. [Available online at <https://ams.confex.com/ams/pdfpapers/47241.pdf>.]
- Fovell, R. G., and Y. Ogura, 1988: Numerical simulation of a midlatitude squall line in two dimensions. *J. Atmos. Sci.*, **45**, 3846–3879.
- Gallus, W. A., Jr., and R. H. Johnson, 1995: The dynamics of circulations within the trailing stratiform regions of squall lines. Part II: Influence of the convective line and ambient environment. *J. Atmos. Sci.*, **52**, 2188–2211.
- Gilmore, M. S., J. M. Straka, and E. N. Rasmussen, 2004a: Precipitation and evolution sensitivity in simulated deep convective storms: Comparisons between liquid-only and simple ice and liquid phase microphysics. *Mon. Wea. Rev.*, **132**, 1897–1916.
- , —, and —, 2004b: Precipitation uncertainty due to variations in precipitation particle parameters within a simple microphysics scheme. *Mon. Wea. Rev.*, **132**, 2610–2627.
- Hong, S. Y., and J. O. J. Lim, 2006: The WRF single-moment 6-class microphysics scheme (WSM6). *J. Korean Meteor. Soc.*, **42**, 129–151.
- , J. Dudhia, and S. H. Chen, 2004: A reviewed approach to ice microphysical processes for the bulk parameterization of clouds and precipitation. *Mon. Wea. Rev.*, **132**, 103–120.
- , K. S. S. Lim, Y. H. Lee, J. C. Ha, H. W. Kim, S. J. Ham, and J. Dudhia, 2010: Evaluation of the WRF double-moment 6-class microphysics scheme for precipitating convection. *Adv. Meteor.*, **2010**, 707253, doi:10.1155/2010/707253.
- Janjić, Z., 1994: The step-mountain eta coordinate model: Further developments of the convection, viscous sublayer, and turbulence closure schemes. *Mon. Wea. Rev.*, **122**, 927–945.
- Jankov, I., W. A. Gallus Jr., M. Segal, B. Shaw, and S. E. Koch, 2005: The impact of different WRF model physical parameterizations and their interactions on warm season MCS rainfall. *Wea. Forecasting*, **20**, 1048–1060.
- Johnson, A., X. Wang, M. Xue, and F. Kong, 2011: Hierarchical cluster analysis of a convection-allowing ensemble during the Hazardous Weather Testbed 2009 Spring Experiment. Part II: Ensemble clustering over the whole experiment period. *Mon. Wea. Rev.*, **139**, 3694–3710.
- Kain, J. S., and Coauthors, 2008: Some practical considerations regarding horizontal resolution in the first generation of operational convection-allowing NWP. *Wea. Forecasting*, **23**, 931–952.
- Kessler, E., 1969: *On the Distribution and Continuity of Water Substance in Atmospheric Circulations*. Meteor. Monogr., No. 32, Amer. Meteor. Soc., 84 pp.
- Klimowski, B. A., M. R. Hjelmfelt, and M. J. Bunkers, 2004: Radar observations of the early evolution of bow echoes. *Wea. Forecasting*, **19**, 727–734.
- Lim, K. S. S., and S. Y. Hong, 2010: Development of an effective double-moment cloud microphysics scheme with prognostic cloud condensation nuclei (CCN) for weather and climate models. *Mon. Wea. Rev.*, **138**, 1587–1612.
- Lin, Y. L., R. D. Farley, and H. D. Orville, 1983: Bulk parameterization of the snow field in a cloud model. *J. Climate Appl. Meteor.*, **22**, 1065–1092.
- Liu, C., and M. W. Moncrieff, 2007: Sensitivity of cloud-resolving simulations of warm-season convection to cloud microphysics parameterizations. *Mon. Wea. Rev.*, **135**, 2854–2868.
- Luo, Y., Y. Wang, H. Wang, Y. Zheng, and H. Morrison, 2010: Modeling convective-stratiform precipitation processes on a mei-yu front with the Weather Research and Forecasting model: Comparison with observations and sensitivity to cloud microphysics parameterizations. *J. Geophys. Res.*, **115**, D18117, doi:10.1029/2010JD013873.
- McCumber, M., W. K. Tao, J. Simpson, R. Penc, and S. T. Soong, 1991: Comparison of ice-phase microphysical parameterization schemes using numerical simulations of tropical convection. *J. Appl. Meteor.*, **30**, 985–1004.
- Mlawer, E. J., S. J. Taubman, T. D. Brown, M. J. Iacono, and S. A. Clough, 1997: Radiative transfer for inhomogeneous atmospheres: RRTM, a validated correlated-k model for the longwave. *J. Geophys. Res.*, **102**, 16 663–16 682.
- Molthan, A. L., J. L. Case, S. R. Dembek, G. J. Jedlovec, and W. M. Lapenta, 2008: The Super Tuesday outbreak: Forecast sensitivities to single-moment microphysics schemes. Preprints, *24th Conf. on Severe Local Storms*, Savannah, GA, Amer. Meteor. Soc., 17B.3. [Available online at <https://ams.confex.com/ams/pdfpapers/141747.pdf>.]
- Morrison, H., and J. Milbrandt, 2011: Comparison of two-moment bulk microphysics schemes in idealized supercell thunderstorm simulations. *Mon. Wea. Rev.*, **139**, 1103–1130.
- , G. Thompson, and V. Tatarskii, 2009: Impact of cloud microphysics on the development of trailing stratiform precipitation in a simulated squall line: Comparison of one- and two-moment schemes. *Mon. Wea. Rev.*, **137**, 991–1007.
- Nicholls, M. E., 1987: A comparison of the results of a two-dimensional numerical simulation of a tropical squall line with observations. *Mon. Wea. Rev.*, **115**, 3055–3077.
- Rotunno, R., J. B. Klemp, and M. L. Weisman, 1988: A theory for strong, long-lived squall lines. *J. Atmos. Sci.*, **45**, 463–485.
- Rutledge, S. A., and R. A. Houze Jr., 1987: A diagnostic modeling study of the trailing stratiform region of a midlatitude squall line. *J. Atmos. Sci.*, **44**, 2640–2656.
- Schwartz, C. S., and Coauthors, 2010: Toward improved convection-allowing ensembles: Model physics sensitivities and optimizing probabilistic guidance with small ensemble membership. *Wea. Forecasting*, **25**, 263–280.
- Skamarock, W. C., and M. L. Weisman, 2009: The impact of positive-definite moisture transport on NWP precipitation forecasts. *Mon. Wea. Rev.*, **137**, 488–494.
- , and Coauthors, 2008: A description of the Advanced Research WRF version 3. NCAR Tech. Note NCAR/TN-475+STR, 113 pp.
- Steiner, M., R. A. Houze Jr., and S. E. Yuter, 1995: Climatological characterization of three-dimensional storm structure from operational radar and rain gauge data. *J. Appl. Meteor.*, **34**, 1978–2007.
- Stoelinga, M. T., 2005: Simulated equivalent reflectivity factor as currently formulated in RIP: Description and possible

- improvements. 5 pp. [Available online at http://www.atmos.washington.edu/~stoeling/RIP_sim_ref.pdf.]
- Szeto, K. K., and H. Cho, 1994: A numerical investigation of squall lines. Part III: Sensitivity to precipitation processes and the Coriolis force. *J. Atmos. Sci.*, **51**, 1341–1351.
- , R. E. Stewart, and C. A. Lin, 1988: Mesoscale circulations forced by melting snow. Part II: Application to meteorological features. *J. Atmos. Sci.*, **45**, 1642–1605.
- Tao, W. K., and J. Simpson, 1989: Modeling study of a tropical squall-type convective line. *J. Atmos. Sci.*, **46**, 177–202.
- , —, C. H. Sui, B. Ferrier, S. Lang, J. Scala, M. D. Chou, and K. Pickering, 1993: Heating, moisture, and water budgets of tropical and midlatitude squall lines: Comparisons and sensitivity to longwave radiation. *J. Atmos. Sci.*, **50**, 673–690.
- , and Coauthors, 2003: Microphysics, radiation, and surface processes in the Goddard Cumulus Ensemble (GCE) model. *Meteor. Atmos. Phys.*, **82**, 97–137.
- van den Heever, S. C., and W. R. Cotton, 2004: The impact of hail size on simulated supercell storms. *J. Atmos. Sci.*, **61**, 1596–1609.
- van Weverberg, K., N. P. M. van Lipzig, and L. Delobbe, 2011a: Evaluation of moist processes during intense precipitation in km-scale NWP models using remote sensing and in-situ data: Impact of microphysics size distribution assumptions. *Atmos. Res.*, **99**, 15–38.
- , —, and —, 2011b: The impact of size distribution assumptions in a bulk one-moment microphysics scheme on simulated surface precipitation and storm dynamics during a low-topped supercell case in Belgium. *Mon. Wea. Rev.*, **139**, 1131–1147.
- , A. M. Vogelmann, H. Morrison, and J. Milbrandt, 2012: Sensitivity of idealized squall-line simulations to the level of complexity used in two-moment bulk microphysics schemes. *Mon. Wea. Rev.*, **140**, 1883–1907.
- Ward, D., and W. Cotton, 2011: A method for forecasting cloud condensation nuclei using predictions of aerosol physical and chemical properties from WRF/Chem. *J. Appl. Meteor. Climatol.*, **50**, 1601–1615.
- Weisman, M. L., 1993: The genesis of severe long-lived bow echoes. *J. Atmos. Sci.*, **50**, 645–670.
- , W. C. Skamarock, and J. B. Klemp, 1997: The resolution dependence of explicitly modeled convective systems. *Mon. Wea. Rev.*, **125**, 527–548.
- Yang, M. J., and R. A. Houze Jr., 1995: Sensitivity of squall-line rear inflow to ice microphysics and environmental humidity. *Mon. Wea. Rev.*, **123**, 3175–3193.